Journal of Enhanced Heat Transfer 31(3):45–81 (2024)

A COMBINED ACTIVE (PIEZOS) AND PASSIVE (MICROSTRUCTURING) PARTIAL FLOW-BOILING APPROACH FOR STABLE HIGH HEAT-FLUX COOLING WITH DIELECTRIC FLUIDS

A. Narain, D. Pandya, J. Damsteegt, & S. Loparo*

The Michigan Technological University, Houghton, Michigan, 49931, USA

*Address all correspondence to: A. Narain, The Michigan Technological University, Houghton, Michigan, 49931, USA; Tel.: +906-487-2555; Fax: +906-487-2822, E-mail: narain@mtu.edu

Original Manuscript Submitted: 8/13/2023; Final Draft Received: 10/16/2023

Controlled but explosive growth in vaporization rates is made feasible by ultrasonic acoustothermal heating of the microlayers associated with microscale nucleating bubbles within the microstructured boiling surface/region of a millimeter-scale heat exchanger (HX). The HX is 5 cm long and has a 1 cm × 5 mm rectangular cross section that uses saturated partial flow-boiling operations of HFE-7000. Experiments use layers of woven copper mesh to form a microstructured boiling surface/region and its nano/microscale amplitude ultrasonic (~1–6 MHz) and sonic (< 2 kHz, typically) vibrations induced by a pair of very thin ultrasonic piezoelectric-transducers (termed piezos) that are placed and actuated from outside the heat-sink. The ultrasonic frequencies are for substructural microvibrations whereas the lower sonic frequencies are for suitable resonant structural microvibrations that assist in bubble removal and liquid filling processes. The flow and the piezos' actuation control allow an approximately 5-fold increase in heat transfer coefficient value, going from about 9000 W/m²–°C associated with microstructured no-piezos cases to 50,000 W/m²–°C at a representative heat flux of about 25 W/cm². The partial boiling approach is enabled by one inlet and two exit ports. Further, significant increases to current critical heat flux values (~70 W/cm²) are possible and are being reported elsewhere. The electrical energy consumed (in W) for generating nano/micrometer amplitude vibrations is a small percentage (currently < 3%, eventually < 1% by design) of the total heat removed (in W), which is a heat removal rate of 125 W for the case reported here.

KEY WORDS: *enhanced microscale nucleate boiling, critical heat flux, enhanced heat transfer coefficient, flow boiling, electronic cooling, direct-chip liquid cooling*

1. INTRODUCTION

Significantly enhanced but steadied microlayer heating and vaporization rates into nucleating microbubbles within the heated and microstructured boiling region of a millimeter scale hydraulic diameter heat-exchanger (HX) is made possible by imposing ultrasonic (1–8 MHz) vibrations. Microlayers are discussed by Kunkelmann et al. (2012), Zou et al. (2015, 2016, 2018), and Schweikert et al. (2019). The focus of experiments in Fig. 1 is to use enhanced vaporization rates for enhanced nucleate pool boiling (ENB) caused by acoustothermal microlayer heating associated with a nucleating bubble on a substrate that is vibrating at ultrasonic frequencies (f_P) (Fig. 2) imposed by the active piezos in Fig. 1. For the HX in Fig. 1, the superheated substrate area (A_{exp}) exposed to the boiling/nucleating fluid is formed by a specific type of woven meshed-wire mi-

NOMENCLATURE

t	Time (s)	A_{exp}	Fluid exposed area of the microstructured boiling region (m^2)
V_P	Piezo excitation voltage DC (V)	$\delta A_{exp\text{-}active}$	An elemental area of A_{exp} where micronucleation occurs (m^2)
Δt_{ON}	Time over which piezo's f_p was ON (s)	$A_{exp\text{-}active}$	The small fraction of A_{exp} where nucleate boiling occurs
Δt_{OFF}	Time over which piezo's f_p was OFF (s)	f_M	Modulation frequency, $[\Delta t_{ON} + \Delta t_{OFF}]^{-1}$
Δt_{Piezo}	Time for one ultrasonic cycle of piezo (s)	D_μ	Diameter of microstructured mesh wire
$\dot{M}_{C_i}$	Coriolis meter measurements (kg/min), i = 1 to 3	H_μ	Height of microstructured mesh
$\overline{T_T}$	Top mesh temperature (°C)	w_μ	Gap between microstructured wired mesh
$\overline{T_B}$	Average temperature at test section bottom (°C)	HTC	Average heat transfer coefficient (W/m^2–°C)
p_{ts}	Test-section vapor port pressure (in kPa)	$\overline{q}''_{CHF}$	Critical heat flux (CHF) (W/cm^2)
T_{tc}	Test-section vapor port temperature (°C)	$\overline{\Delta T_D}$	Driving temperature difference (°C)
f_P	Piezos resonance frequency $(\Delta t_{Piezo})^{-1}$	Δ_F	Characteristic liquid passage gap-height (μm)
A_{bs}	Heated area at the bottom of the test section (m^2)		

crostructuring (Figs. 1 and 3). A tiny portion of this exposed area, A_{exp}, which is active ($\delta A_{exp\text{-}act}$) and sees bubble formation and dislodging motions, with or without ultrasonic heating of the microlayer, are areas around active points P indicated in Fig. 2(a) and 2(b). The ultrasonic vibrations of the individual wires (called a substructure of the bonded sheets of woven mesh forming the microstructured region) are induced by activating one or both ultrasonic piezos that are bonded to the outside HX walls (Fig. 1).

Preliminary 3D laser vibrometry experimental results (Fig. 4) confirm the presence of nano-to-micro-m amplitude ultrasonic vibrations over the entire meshed boiling region (Figs. 1 and 3a). The lower sonic frequencies f_M (< 10 kHz), superposed as amplitude modulations of the driving ultrasonic signals (Fig. 1c), are used to induce resonant structural microvibrations (i.e., of the mounted test section along with the entire HX in Fig. 1) at one of the natural vibration modes (identified in Fig. 5 by a chirp-excitation modal analysis). Consequently, the mechanical power needed for sustaining sonic f_M vibrations is small and of low amplitudes. Also, the electrical power consumed by the R-f amp (Fig. 1) associated with these frequencies f_M is minuscule (a factor of about 10^{-4} of the piezos power associated with the frequencies f_P). Furthermore, the piezos consume a small amount of power to excite the crystal vibrations at f_P because of smart and efficient R-f amp operations at an antiresonance f_P value as identified by an *in situ* impedance-frequency characterization of the electromechanical coupling in Fig. 1 (see APC International, 2002). The resonant micron-scale structural microvibrations' amplitudes can be measured from accelerometers. Amplitudes associated with both structural and substructural microvibrations can also be measured (off the flow-loop) by the same 3D laser vibrometer used for the results in Fig. 4.

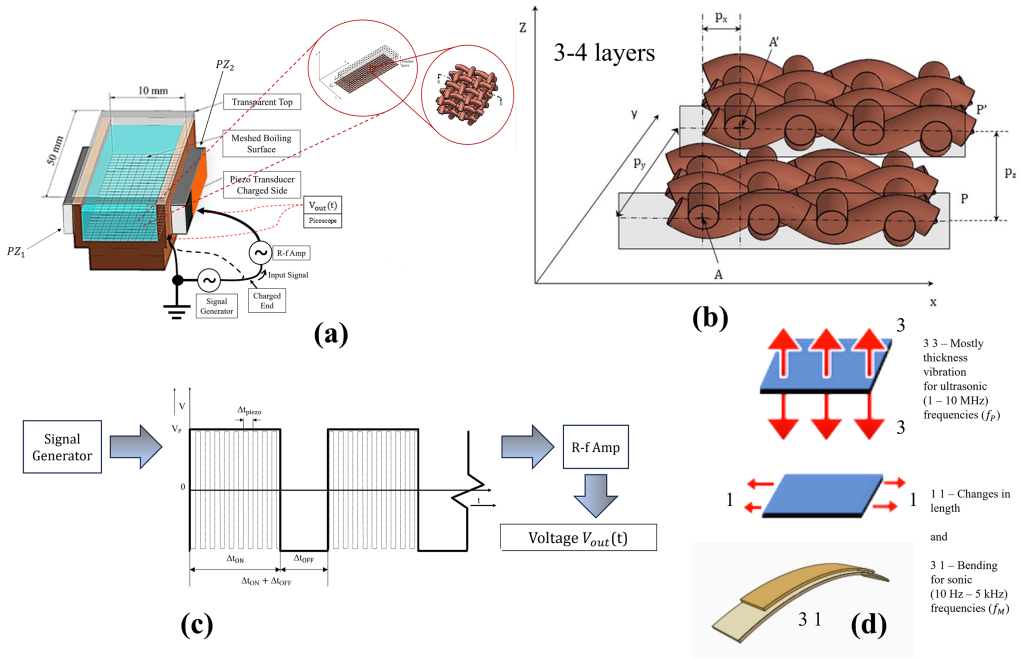

FIG. 1: (a) A representation of piezos and a single minichannel (SC) with a sample depiction of the 3D microstructuring of the boiling surface and piezos placement outside the channel. Here four sheets of woven copper are diffusion bonded to each other and to the plain copper surface at the channel bottom. (b) A representative pair of woven copper sheets can be diffusion bonded together at different offsets p_x and p_y, respectively, in the x and y directions. The two sheets come into contact, with $p_z = 0$, at contact points or contact lines, which depend on p_x and p_y values (here wavy wires' centerlines peak-to-peak distance is $\lambda \cong 500$ μm, and the wavy wires' centerlines peak-to-peak amplitude equals wire diameter $D_\mu \cong 114$ μm). (c) The voltage signal output from the signal generator is a square wave signal with an ultrasonic high-frequency $f_P \equiv [(\Delta t_{Piezo})]^{-1} \cong 1$–5 MHz superposed with a low-frequency square wave amplitude modulation (doubling the original ultrasonic square-wave amplitude) frequency $f_M \equiv [(\Delta t_{ON} + \Delta t_{OFF})]^{-1}$(typically < 10 kHz). The f_P value is chosen to be at the antiresonance frequency of the piezo. (d) The ultrasonic f_p frequencies typically excite 3-3 mode thickness vibrations and sonic f_M mode typically excites both 1-1 (extension-contraction) and 3-1 bending mode) vibrations of the piezos.

The fact that the substructural vibrations (Fig. 4) at ultrasonic frequency f_P induce acoustothermal heating of the microlayers, as indicated in Fig. 2, is deduced and discussed in the thin film evaporation studies of Pillai et al. (2018) and Datta et al. (2021). With the help of other mechanisms discussed later, the sonic microvibrations f_M assist in creating suitable hydrodynamics for bubble removal and liquid-filling processes within the nucleate-boiling region of the stagnant fluid trapped in the microstructure of Fig. 3. For chip-cooling applications, flow-boiling of Novec 3M Engineered fluids (HFE-7000 in completed experiments and Novec 646 in ongoing experiments) in this HX study are meant to advance current liquid-cooling approaches in practice (Rangarajan et al., 2023). For this mm-scale HX and the associated macroscale flow-loop, steady flows (over time scales > 0.1 s) are realized by suppressing various HX [e.g., critical heat flux (CHF); Carey et al., 2018; Faghri and Zhang, 2006; Qu and Mudawar, 2003; Tamvada et al., 2021; Liu et al., 2022] and system-level instabilities (Chiapero et al., 2012; Maulbetsch and Griffith, 1966; Kakac et al., 2008; Bhatt and Wedekind, 1980).

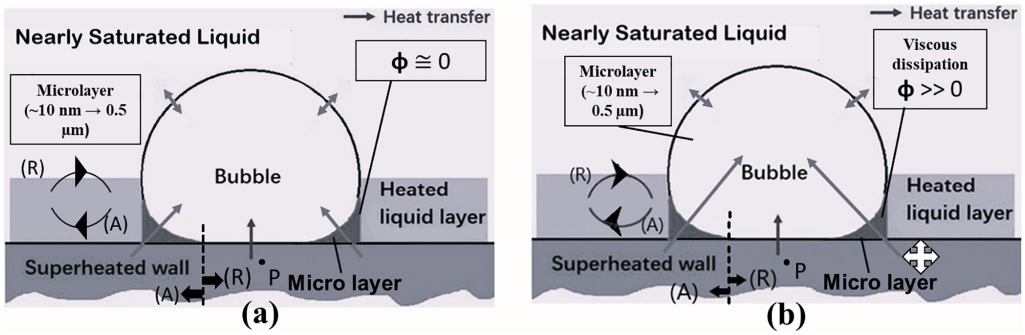

FIG. 2: (a) The microlayer of a randomly selected nucleating bubble at an active substrate location P (also see Fig. 3a) over its advancing/receding duration carries 80–90% of the total heat removed by the bubble (Kunkelmann et al., 2012; Schweikert, et al., 2019; Kim, 2009). (b) Significant enhancement of vaporization rates into the same bubble, as indicated by the larger micro layer to bubble arrow, is likely due to the substrate's ultrasonic vibrations (indicated by white cross arrows) that acoustothermally heat the microlayers.

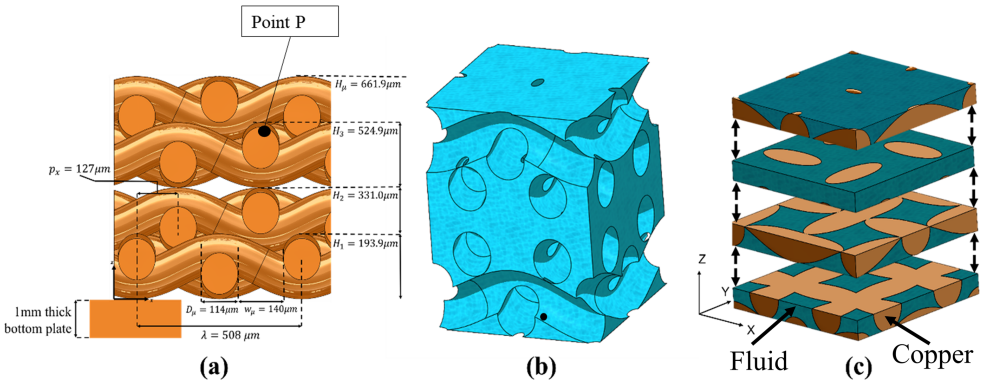

FIG. 3: (a) An x–z cross section of a specific 4-layered mesh (defined later), indicated in Fig. 1a–1b, used here. Of the 5 cm × 1 cm mesh covering the bottom surface (x–y plane), the cross section shown is of a λ(500 μm) × λ × 662 μm 3D region. Here λ is the indicated wavelength of the wires center line, and H_μ = 662 μm is the maximum height of the micro structure. (b) Depiction of the λ × λ × 662 μm simply connected 3D fluid-filled region with copper wires shown as holes. (c) Cut sections at representative z-locations (of certain thicknesses) of the 3D region showing the copper and the fluid.

Among other applications, the approach described here is likely to enable next-generation chip cooling in servers, racks, and data centers (Narumanchi et al., 2012; Waye et al., 2014). This could potentially upgrade existing liquid cooling (Rangarajan et al., 2023; DCLC & D2C Liquid Cooling Technology Vendors, n.d.) or ENB approaches (ZutaCorp, n.d.). This is possible because the clean and closed flow-loop approach described here has met, or is on the way to meeting, the following list of criteria that must be concurrently met. (1) The fluid used should have a global warming potential of around one and ozone depletion potential of nearly zero, be electronics-friendly, and preferably have a boiling point of around 40–50°C near atmospheric pressures. A dielectric fluid, 3M Inc.'s Engineered Fluid Novec 649 (similar to Novec HFE-7000 used here), or comparable fluids, meet these environmental criteria. (2) The boiling-surface/region microstructuring should use materials that are thermally conducting and deploy patterning that is manufacturable, scalable, durable, and economi-

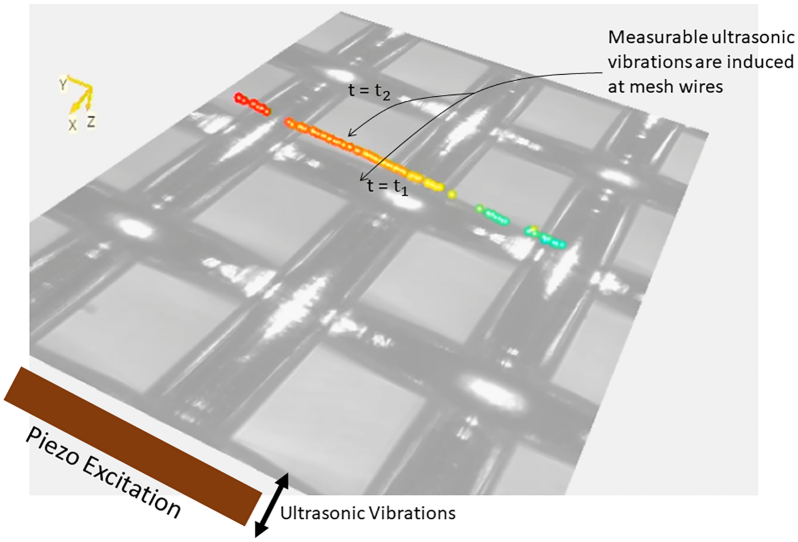

FIG. 4: Preliminary experiments conducted at Polytec, 3D lab for copper mesh in Fig. 1 support the conclusion that substructural ultrasonic vibrations (nm/µm amplitudes and frequencies in the 1–8 MHz range) are measurable with the help of 3D Laser Vibrometry from Polytec 3D. Each mesh wire's motion, indicated by wires' instantaneous positions at time instants t_1 and t_2 (the wire widths are the same though they look different at the two instants because of camera effects), is due to the piezos' ultrasonic excitation. More complete characterizations of the entire stack of wires in Fig. 3(a) are part of the ongoing project.

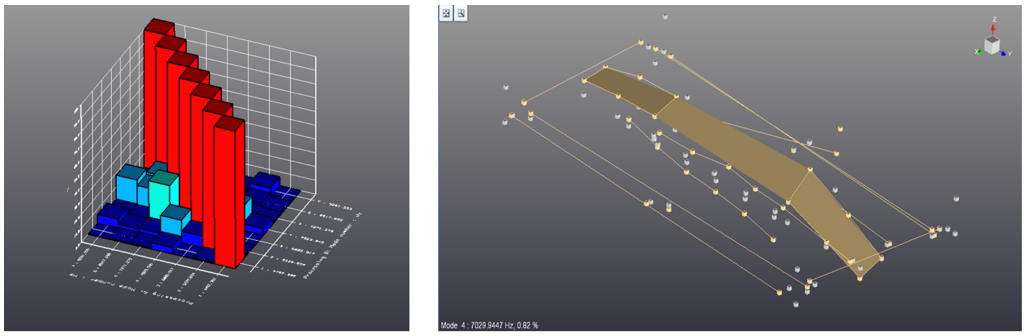

(a) **(b)**

FIG. 5: (a) The natural presence of the structural microvibrations is ascertained as shown by chirp-excitation–based modal analysis. Depending on the imposed modulation frequency f_M in Fig. 1(c), one of the different mode shapes (as ascertained in part b of the figure) will be in resonance and emphasized. The vertical axis in the figure indicates a higher degree of correlation with the mode shapes (taller blocks) along the diagonal of the frequencies shown in the horizontal plane of this figure. Off-diagonal mode shapes are not relevant. (b) A set of triaxial accelerometers are located at different points (indicated by dots in the figure) at the bottom of the test section HX. The measurements are taken after mounting/embedding the test section assembly in the flow loop. These measurements yield the results in (a). This sample mode #4's instantaneous configuration is shown here and it exhibits a predominantly up-and-down transverse motion associated with frequency f_M ~7 kHz along the diagonal.

cally feasible. (3) Active enhancement should lead to high heat transfer coefficient (HTC) values (~40–60,000 W/m^2–°C or more) available for a range of heat fluxes (10–150 W/cm^2 or more) of interest, with CHF greater than 150–200 W/cm^2 or more. (4) The approach should allow high power density (~50 MW/m^3 or more) for a small volume (~10 cm^3 or less) of the millimeter-scale HX under reliable electronic packaging. (5) The HX pressure drop and pumping power requirements should be small and within acceptable limits. (6) The HX design should also allow waste heat recovery, energy efficiency, and economic advantages, preferably under doable modifications of existing approaches (e.g., for data centers, at server, rack, and data center power supply levels).

1.1 Brief Literature Review

Relevant flow-boiling literature is vast and is briefly categorized here. Existing knowledge and investigations for traditional flow-boiling operations involving all liquid flow at the inlet and nearly all vapor flow at the exit that utilizes micrometer-to-millimeter–scale hydraulic diameter channels have not yielded sufficient heat-flux capabilities for acceptable steady operations that meet the needs of closed-loop operations for cooling of high power density electronics in emerging technologies (Carey, 2018; Faghri and Zhang, 2006; Kandlikar, 1990; Kenning et al., 1989; Chen, 1966; Chen and Jebson, 1997). At desired high heat fluxes for dielectric fluids, these traditional operations (with or without microstructuring) yield unacceptable performances. Examples of unacceptable performances for electronics-friendly engineered fluids are large pressure drops (Kim et al., 2013; Lee and Mudawar, 2005; Wu and Chen, 2003; Qu and Mudawar, 2003), low HTCs such as 5000–15000 W/m^2-°C, and CHF values less than 50–60 W/cm^2 (Tamvada et al., 2021). Other performance problems to be avoided are instabilities due to causes outside the heat sink at the system level (Bhatt and Wedekind, 1980; Zhang et al., 2006; Weisman and Pei, 1983; Hewitt, 1978). Instabilities at the HX level such as CHF instability in passive approaches (Qu and Mudawar, 2004; Zhang et al., 2006; Weisman and Pei, 1983; Hewitt, 1978; Tamvada et al., 2021) or in the active enhancement approaches (e.g., in the electrical power drive indicated in Fig. 1a or in Bozink et al., 2017) also need to be suppressed or delayed to achieve good HX performance. The causes of system-level instability (Chiapero et al., 2012; Maulbetsch and Griffith, 1966; Kakac et al., 2008; Bhatt and Wedekind, 1980) when an HX is put in a closed flow loop may vary depending on the nature of the external system. Some well-known causes are (1) performance problems due to cavitation (Zhou et al., 2014; Cheesewright et al., 2000) within the devices (gear pumps and Coriolis meters) or just upstream of their inlets, (2) the external system's pressure drop requirements vis-à-vis capability of the pumps used and valve-adjusted flow resistances that are available (especially in the liquid lines), (3) type of flow control used and condenser sections' heat removal rate capabilities that also have a bearing on whether or not condenser instabilities can be suppressed, and so on. For the system and the flow control used in this paper, all relevant instabilities have been suppressed or delayed (Pandya et al., 2023a,b). For flow/pool-boiling, enhanced heat removal performance has been vigorously investigated (with a greater focus on pool-boiling) by employing different types of microstructured surfaces (Chu et al., 2013; Wen et al., 2017, 2018; Thiagarajan et al., 2015); some have also investigated active piezos-induced enhancement approaches (Heffington and Glezer, 2004; Swarnkar and Lakhera, 2021; Douglas et al, 2012; Shariff, 2011) with a primary focus on acoustic/ultrasonic dislodging of nucleating bubbles in ways different than the substrate vibrations used and described here (Fig. 2) where the focus is both on additional vaporization into nucleating bubbles within a micro-structured region as well as enhanced bubble removal and liquid refilling processes.

2. MOTIVATION AND BACKGROUND KNOWLEDGE FOR A NEW EXPERIMENTAL APPROACH

The potential success of concurrent impositions of ultrasonic and sonic microvibrations on the substrate forming the boiling surface is hypothesized and experimentally demonstrated

here. The hypothesis is also supported by molecular dynamic simulations-based results with scaled-up continuum-level interpretations concerning enhanced thin film evaporations under acoustothermal heating (Pillai et al., 2018; Datta et al., 2021), but for the first time applied here to dynamic nucleating bubbles' microlayers. These simulations suggest that mesh-wire vibrations associated with ultrasonic excitations will likely lead to heating of the microlayers of the nucleating bubbles (Fig. 2) whose departure diameters are much less than the characteristic fluid-filled gap size of the microstructure (Fig. 3), defined as Δ_F, which equals the ratio of fluid volume filled in the microstructure to the surface area, A_{exp}, of the meshed microstructure that is exposed to the fluid (therefore, in Fig. 3, Δ_F ~48 μm). This microlayer heating (Fig. 2) is possible because, as Pillai et al. (2018) suggest, the Stokes boundary layer thicknesses ($\Delta_{BL} \equiv \sqrt{\frac{\mu}{\rho(2\pi f_P)}} \approx 0.9$ μm for HFE-7000 at 5 MHz) associated with the substrate microvibrations, within which viscous dissipation cannot be ignored, is of the order of magnitude of the microlayer thicknesses because they have to be much less (~1/100th or less) than the fluid-filled gap thickness Δ_F (~48 μm) within which bubbles are formed and dislodged. This situation should cause substrate's ultrasonic vibrations to lead to acoustothermal heating (Pillai et al., 2018; Datta et al., 2021) of the bubbles' microlayers while still avoiding other unwanted phenomena (such as nucleate boiling, film boiling, or cavitation phenomena within the microlayer in Fig. 2) associated with too much vibratory heating. Such unwanted phenomena are avoided because a certain nondimensional parameter, defined as A* in Pillai et al. (2018), is kept small. This parameter is dependent on the frequency and amplitude of the ultrasonic vibrations along with fluid properties (such as its molecular weight and temperature, which measure thermal agitation; and fluid viscosity and density, which affect viscous damping) and its smallness criterion defines when a certain combination of the amplitude and frequencies of the ultrasonic vibrations are low enough to cause evaporations only at the liquid–vapor interface of the microlayer in Fig. 2. Analogous continuum scale enhanced evaporation (into the atmosphere) of microdroplets of liquid in fabric fibers, subjected to piezos-induced ultrasonic vibrations, have earlier been experimentally observed (Peng et al., 2017) and attributed, by molecular dynamic simulations (Pillai et al., 2018), to the very same acoustothermal heating.

The preliminary 3D laser vibrometry experiments for the mesh in Fig. 1 are performed by Polytec, Inc. in its lab using its MSA-100-3D vibrometer; results are shown in Fig. 4. It shows that the ultrasonic 3-3 vibrations (Fig. 1d) induce substructural vibrations of the mesh wires, and their amplitudes rise with increasing electric power supplied by the drivers. Experimental results for the actual meshed test section and the various frequencies and amplitudes of the mesh wires are not central to the paper but are planned through follow-up experiments.

Preliminary experimental results in Fig. 5, using the chirp-excitation method (Schwarz and Richardson, 1999) and placement of accelerometers on the bottom of the test section in Fig. 1(a), support the fact that low-frequency sonic vibrations, when imposed at ever-so-low power levels through the piezos driving arrangement in Fig. 1, will lead to resonant structural vibrations (very low amplitudes) of mode shapes consistent with the energy available at the chosen f_M value in the 10–10,000 Hz range. This range of sonic structural vibration can provide Bjerknes forces (see Boziuk et al., 2017) to be in resonance with frequencies associated with bubble formation and dislodging time scales (Bigham et al., 2018).

3. EXPERIMENTS

3.1 Experimental Approach

The flow boiling experiments involving HFE-7000 use the test section shown in Fig. 6. Reported experimental results also relate, through nondimensional numbers defined in Narain et al. (2018), to flow boiling of 3M Novec's engineered fluids such as HFE-7000/Novec 649 (although reported data here are only for HFE-7000). The nondimensional results are to be presented else-

where (Pandya, 2023b). These experiments are used here to reconfirm realizations of earlier reported high heat flux and highly efficient active/passive enhanced micronucleation flow-boiling (Narain et al., 2022, 2023) in the novel and better instrumented single-channel HX arrangement of Fig. 1. The HFE-7000 is boiled with the help of a single heating block made of copper (which is heated by cartridge heaters with a sufficient rated capacity of supplying up to 1200 W of heat to the test section). Figures 6–9 describe the setup. The well-defined microstructure and pore

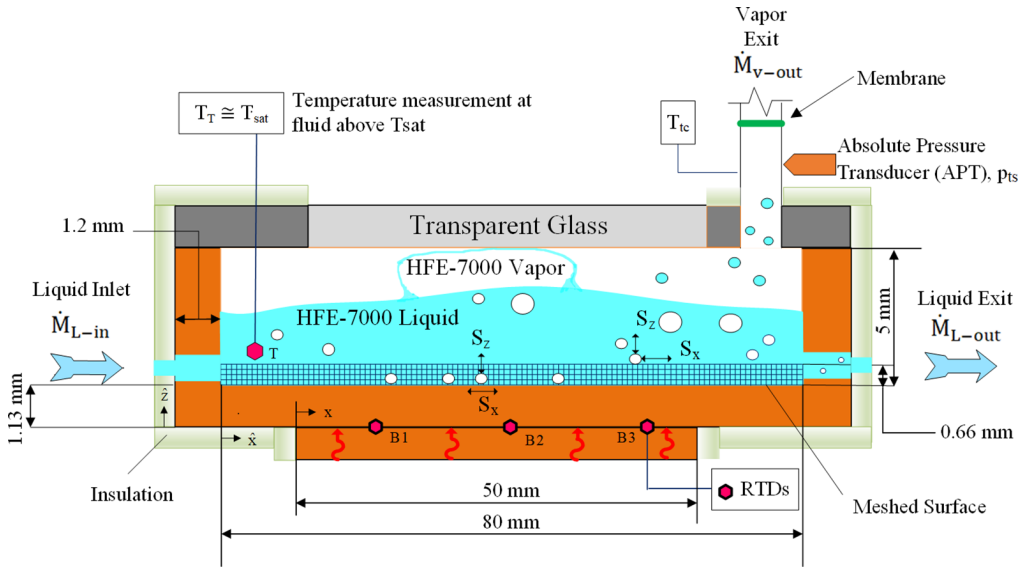

FIG. 6: Inlet to outlet longitudinal view and dimensions of the test section and its instrumentation for the reported experimental results

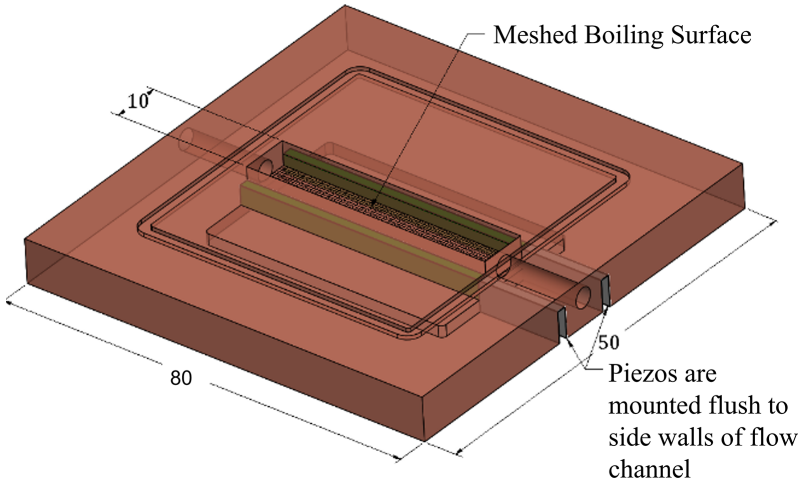

FIG. 7: 3D view of the copper block (dimensions are in mm) of heatsink with single channel test section of dimensions 8 cm × 1 cm × 5 mm, as in Fig. 6 (with a centrally heated area A_{bs} = 5 cm × 1 cm, embedded in the center) with piezos mounted within the slots outside

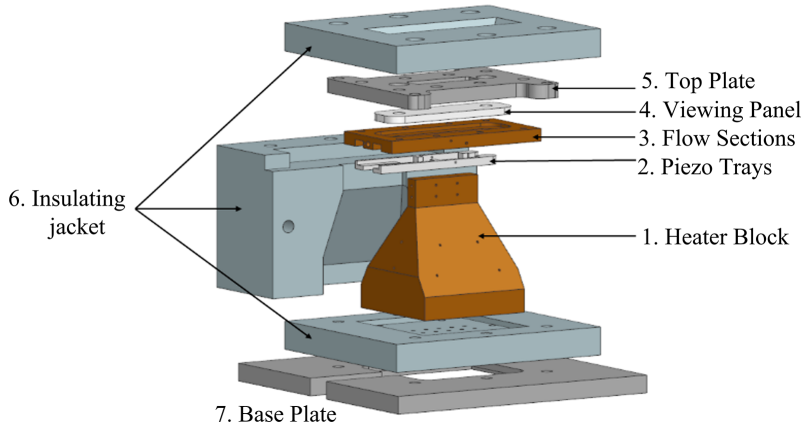

FIG. 8: Heater block test section assembly used in the flow loop (see Fig. 9)

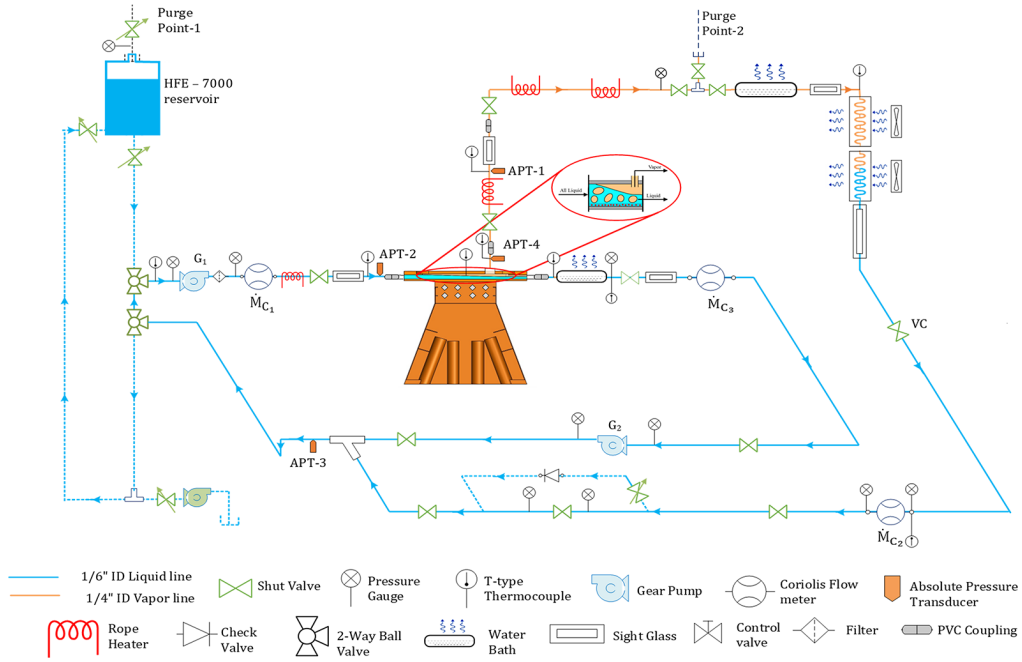

FIG. 9: An outline of a revised representative flow loop

sizes of single layers of mesh used here are by themselves Wenzel filling (Wen et al., 2017; Erbil and Cansoy, 2009; Murakami et al., 2014). When bonded together, they form the microstructure choices (Figs. 1 and 3) used here, and fluid filling and emptying operations in them are partially enabled by the structural microvibrations discussed in Fig. 5 along with other flow physics issues (pumps fluid for injection/suction, etc). The two hard PZT piezos (from APC, Inc.) in Fig. 1(a) are bonded semipermanently or permanently (see Pandya, 2023b) and then fired at high ultrasonic crystal frequencies, f_{P1} and f_{P2} (possible in 1–8 MHz, but ~5 MHz chosen here) at their nearby antiresonant frequency f_{AR} values (see APC International, 2002) that account for excita-

tion at energy efficient natural crystal frequencies in the context of Piezos' electromechanical coupling to the structure it vibrates with. In Fig. 10, f_{AR} is 4.73 MHz, and the magnitude of the impedance Z has a maximum value). At this frequency, the PZT has 3–3 thickness mode vibrations that are dominant (Fig. 1d), and the electromechanical vibrations, as modeled by the PZT electrical circuit (APC International, 2002) that the R-f amp in Fig. 1 sees, is quite efficient (mostly reactive with a low resistive component of Z). The sample impedance-frequency characterizations (Z–f) for PZ_1 in Fig. 1(a), as shown in Fig. 10, are obtained after mounting the test section assembly in the flow loop of Fig. 9. Figure 10 results were obtained from an impedance meter (Keysight Technology's Model E4990A). The input signals out of the signal generator (SIGLENT Technology's SDG1032X) in Fig. 1(c) are amplitude-modulated (modulation index of 1) square waves (preferred after testing other waveforms, including sinusoids) at modulation frequencies of f_{M1} and f_{M2} (in 0–10 kHz range), respectively. The HFE-7000 vapor from the test section's predominantly vapor exit port (feeding into the line in Fig. 9 where APT1 is placed) goes through curvy tubing with rope heaters that vaporize most of the entrained liquid droplets. The subsequent onward flow of slightly superheated vapor in this line is steadily condensed using a water bath (a precondenser) followed by the two air-cooled condensers indicated in Fig. 9. A representative sight glass location placed right after the last of the condensers (see Fig. 9) visually monitors and ensures that the flow further downstream is a single-phase liquid flow (with monitored pressure-temperature conditions conducive to inhibiting cavitation at the Coriolis meter that measures $\dot{M}_{C_2}$). The predominantly liquid exit port of the test section sees purely liquid flow, after it condenses any entrained vapor in the water bath, in the line leading to the Coriolis meter (that measures $\dot{M}_{C_3}$) and the gear pump G_2. Again, valve control with monitored pressure-temperature conditions ensures no cavitation within or upstream of the Coriolis meter $\dot{M}_{C_3}$ and the gear pump G_2. These two liquid streams are merged into a single liquid stream with the help of the gear pump G_1 used to feed the liquid HFE-7000 into the test section inlet (Fig. 9) at a desired mass flow rate set for the Coriolis meter $\dot{M}_{C_1}$ that would leave a sufficient amount of unvaporized liquid by the exit of the test section (for a given heat load supplied by the heater

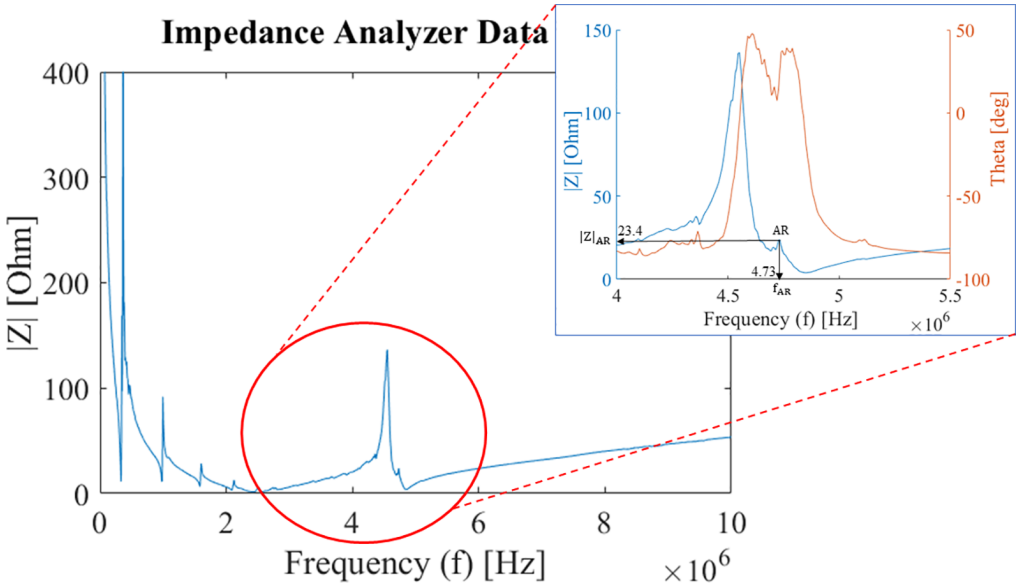

FIG. 10: The |Z|-f-θ_Z curve for one representative piezo PZ_1 in Fig. 1, obtained by impedance meter

block in Fig. 8). The gear pump G_2 in Fig. 9 is also used as a control to rapidly attain the natural mass flow rates associated with the steady values of approximately separated liquid and vapor flow rates (at the two exits of the test section in Fig. 6) that add up to the desired mass flow rate $\dot{M}_{C_1}$ at the test section inlet. The left side inventory control HFE-7000 reservoir shown in Fig. 9 is used when needed. It can store, at any instant, twice the quantity of the liquid flowing in the flow loop. A controllable rope heater between pump G_1 and the test section is used to ensure that the liquid HFE-7000 entering the test section is near the desired saturation temperature (though slightly subcooled by 1–2°C) associated with the steady test section pressure.

3.2 Experimental Setup

The test section is machined into the center of a 5 cm × 5 cm × 1 cm copper block (Fig. 7) mounted on a heater block wrapped in insulation (Fig. 8) and deployed in a flow loop (Fig. 9) with features that allow suitable measurements and flow control.

The piezos, as shown in Fig. 1(a), are mounted on the outside of the flow channel. This is accomplished by carving out adjacent slots in the copper block (see Fig. 7). The flow channel's bottom surface for the test sections has an approximate 0.66 mm thick meshed surface [see Figs. 3(a) and 6] whereas the planar bottom and side walls of copper in Fig. 6 are, respectively, 1.13 mm and 1.2 mm thick.

3.2.1 Two Test Section Outlets for Approximate Phase Separation

The two test-section exit ports (Figs. 6 and 9) achieve approximate phase separation by virtue of the design of resistance to the vapor flow through the liquid-filled pores of the microstructure feeding into the liquid lines and negligible resistance to the vapor flow through the larger diameter predominantly vapor exit ports (there are other features in the upcoming test sections that further enhance CHF). The main feature and benefit of this approach is extremely low-pressure drop (between the inlet and the exits of the test section), even for very high heat-flux operations involving significant vapor volume flow rates. This is because nucleate boiling sets up transverse pressure drops (from the microstructured boiling surface to the predominantly vapor exit port) that the test section design is able to use for efficient management of vapor flows. Another advantage of such designs is the potential of their efficacy (with minor changes) in multi-g or zero-g environments.

3.2.2 Microstructuring

The meshed microstructure is obtained from diffusion bonding of four layers of a suitable woven copper mesh (in this example, a square-shaped 100 mesh from TWP, Inc.) of dimensions reported in the caption of Fig. 1: 100 copper wires per 2.54 cm (each wire is of 114 μm diameter and the weave in a single layer along the z direction of Fig. 1b forms 140 μm sided square holes between a crossed pair of woven wires). The $\lambda \times \lambda \times 4$-layer block cross section in the x–z plane, with λ at 500 μm, shown in Fig. 3(a) is created in Solidworks (and is approximately the same as the actual geometry assessed under LEICA DVM6 digital microscope). The distances $p_x \approx \lambda/4 = 127$ μm, and $p_y \approx \lambda/4 = 127$ μm between layers 1 and 2 are arranged on top of the bottom boiling plate in Fig. 3(a), and they lead to a maximum height $H_2 = 331.0$ μm after the two layers have touched each other and the bottom plate in the z-direction. The micro-structure has $p_x \approx 0$ μm, and $p_y \approx 0$ μm between layers 2 and 3, and has $p_x \approx \lambda/4 = 127$ μm, and $p_y \approx \lambda/4 = 127$ μm between layers 3 and 4. The total z-height of layers 2 and 3 is also 331.0 μm whereas the total maximum z-height of the mesh is $H_4 = 662$ μm. For this specific microstructure, the total exposed-to-fluid heated surface area $A_{exp} = 6.729$ m^2, fluid volume = 326.4 cm^3, and characteristic fluid passage thickness Δ_F at 48 μm. In earlier experiments (Narain et al., 2022, 2023), other mesh structures have also

been successfully tested; after more tests, suitable qualitative and quantitative microstructural choice recommendations are expected to be reported in forthcoming works.

3.2.3 Test-Section and Flow-Loop Instrumentation

The experiment here uses the flow loop in Fig. 9. The setup has a boiling test section, Coriolis flow meters, absolute pressure transducers, temperature sensors, and cartridge heaters (embedded in the heater block of Fig. 8) that provide the heat to the test section bottom (the surface of 50 mm length—containing points B1, B2 and B3 in Fig. 6), power meters for the cartridges, a precondenser bath and two air-cooled condensers for the vapor line, a condenser water bath, a predominantly liquid exit line of the test section, two gear pumps, a reservoir, copper tubing, superheating or temperature-control rope heaters, and various other accessories/devices. Other accessories include bonded piezos, piezo drivers, one-way valves, two-way valves, shut-valves, filters, and so on, and signal/power inputs to certain devices as well as NI data acquisition (DAQ) systems for acquiring crucial data through suitable DAQ systems. This data allows flow control and quantitative analysis of heat transfer rates for this mini channel HX made of copper.

3.3 Experimental Procedure for Startup, Inventory, and Flow Control for Steady State Operations

The flow-loop hardware in Fig. 9 has been strategically chosen, and the fluid chambers are gravity-filled (could be pump-filled) with liquid from the reservoir before being partially emptied with suitable inventory control (to the desired liquid volume and liquid temperature in the heat-sink zone). Subsequent startup and control procedures are defined and tested for stable flow-boiling realizations at high heat flux. These are described in Pandya et al. (2023a,b) and are omitted here for brevity.

The flow loop in Fig. 9 is readied after using compressed air for leak tests, liquid filling, and de-aeration (pressure-purging several times to make the L/V phases nearly free of air and noncondensable gases) processes through suitable transient operations. The DAQ and flow control lead to highly efficient and controlled flow-boiling with stable operations. Using gear pump G_1, the steady-in-the-mean inlet mass flow rate $\dot{M}_{L-in} = \dot{M}_{C_1}$ (all Coriolis meter readings $\dot{M}_{C_1}$, $\dot{M}_{C_2}$, and $\dot{M}_{C_3}$ in Fig. 9 are obtained in real time, and relevant steady-in-the-mean values are obtained) is adjusted for a given heat load q_{bs} (in W) entering the test section over its boiling-surface area A_{bs}, until we achieve a desired inlet liquid flow rate $\dot{M}_{C_1}$ that satisfies a certain condition, $\dot{M}_{c_1} \cong \dot{M}_{c_2}/X_e$, where X_e is typically a number in the 0.4–0.6 range. The minimum inlet mass flow rate $\dot{M}_{L-in}$ is termed $\dot{M}^*_{L-in} \equiv q_{bs}/h_{fg}$, which is a value that will get completely vaporized for a given heat input in the test section. It also equals the total vapor mass flow rate out of the two ports (one predominantly vapor and one predominantly liquid) under partial boiling conditions for which we define exit vapor quality $X_e \equiv \dot{M}^*_{L-in}/\dot{M}_{L-in}$ (see Pandya et al., 2023a). Here $q_{bs} = q''_w * A_{bs}$, where average heat-flux q''_w (W/m^2) is the ratio of the heat added q_{bs} over the boiling-surface area A_{bs}, and h_{fg} is the fluid's heat of vaporization—in J/kg—at the test-section pressure p_{ts} (measured by APT1 in Fig. 9). Partial flow-boiling operations are chosen with exiting vapor flow-rate quality X_e self-selected to be some subset (based on hardware constraints) in the range of 0.4–0.6 (say $X_e \cong 0.5$) by running the incoming liquid line gear pump G_1 to satisfy this suitable $\dot{M}_{C_1} \cong \dot{M}_{c_2}/X_e > \dot{M}_{C_2}$. Further, there are well-defined transient approaches that allow reaching a steady state near selected test-section pressure p_{ts}. Steady-state operations are achieved in a small duration of time through the control of gear pump G_2 to achieve $\dot{M}_{c_3}$ values that actively attempt to satisfy the desired steady flow mass balance $\dot{M}_{c_1} = \dot{M}_{c_2} + \dot{M}_{c_3}$, which is verifiably satisfied after steady state is attained (accounting for subsequent vaporization of any calculated/estimated liquid entrained rate in the exiting vapor line and/or vapor entrainment rate condensed in the exiting liquid line).

3.4 Piezos Power Consumption

It is vitally important to know the total dissipative (i.e., resistive) power P_{PZ-t} (in W) used in driving the piezos for each run where the HX is removing a certain amount of heat q_{bs} (in W) from the heat source [here the heat source from which the heat enters HX along the line connecting the resistance temperature detector (RTD) locations B_1, B_2, and B_3 in Fig. 6]. This is because, for this active ENB cooling approach, the use of piezos must lead to a quantifiably small piezo-use effectiveness parameter defined as

$$\varepsilon_{PZ} \equiv \frac{P_{PZ-t}}{q_{bs}} \tag{1}$$

Currently, $\varepsilon_{PZ} \le 0.03$ and $\varepsilon_{PZ} \le 0.01$ is expected soon. Such small values are made possible (see the Appendix and APC International, 2002) by driving the piezos at their antiresonance frequency f_{AR}, identified in Fig. 10 and its inset with the help of $|Z| - f$ curves obtained by an impedance meter. Besides being able to obtain ε_{PZ} through suitable measurements of voltage and impedance associated with the piezos in Fig. 1, it is also important to obtain (see the appendix) the power spectral density function, psd(f), to obtain the different amounts of piezos' power used in different frequency spectrum windows of interest (e.g., windows around the driving ultrasonic frequency f_p, around substructural ultrasonic vibration frequencies where the wires actually vibrate as assessed by 3D laser vibrometry, and around the sonic modulation frequency f_M associated with the resonant structural vibrations).

3.5 Uncertainties

Standard uncertainty calculation procedures (Coleman et al., 1999; Moffat, 1985) for a measured time-varying sensor variable v(t) are followed. Variable v(t)'s discretized values at times t_i [assume a 10 Hz DAQ sampling rate for most sensors, 10 Hz or 3000 Hz (planned) for APT-2 and APT-4 in Fig. 9, and 125 MHz for V_{out} (t) in Fig. 1] with $1 \le i \le N$, over a suitable time interval, is defined as $v_i \equiv v(t_i)$. The steady-in-the-mean value of v_i over this interval is denoted as $\bar{v}_i$. Factory and lab calibrations for thermocouples and pressure transducers (APTs) are conservatively put in the fixed $\left(U_{\bar{v}_i}^{\text{fixed}}\right)$ category defined below. The statistical uncertainty for each variable is put in the uncertainty $\left(U_{\bar{v}_i}^{\text{variable}}\right)$ category defined below (the formula assumes a 68% confidence level; Coleman et al., 1999). The uncertainties for the average of each variable are reported as $\bar{v}_i \pm U_{\bar{v}_i}$.

$$U_{\bar{v}_i} = \left[\left(U_{\bar{v}_i}^{\text{fixed}}\right)^2 + \left(U_{\bar{v}_i}^{\text{variable}}\right)^2\right]^{1/2} \tag{2}$$

$$U_{\bar{v}_i}^{\text{fixed}} = \left[\left(U_{\bar{v}_i}^{\text{factory}}\right)^2 + \left(U_{\bar{v}_i}^{\text{calibrated}}\right)^2\right]^{\frac{1}{2}} \tag{3}$$

$$U_{\bar{v}_i}^{\text{variable}} = \sigma_{\bar{v}_i} = \frac{\sigma}{\sqrt{N}} \quad \sigma \equiv \left[\frac{\sum_{i=1}^{N}\left(v_i - \bar{v}_i\right)^2}{N-1}\right]^{\frac{1}{2}} \tag{4}$$

3.5.1 Heat Flux and Its Error Estimate

The average heat-flux $\bar{q}''_w$ (W/cm^2) over the boiling surface (of area A_{bs}) was estimated from

$$\bar{q}''_w\left[\frac{W}{cm^2}\right] = \frac{\{q_{watt-meter}[W]\} - \{q_{leakage}[W]\}}{A_{bs}} \tag{5}$$

where $q_{watt-meter}$ is total cartridge power measured by a watt meter and $q_{leakage}[W]$ is the semiempirical estimate of heat leakage from the heater block and the test section's insulated outer surfaces (for details, see Pandya, 2023b). Other methods (based on two-phase energy balances for the test section and associated piping sections) of estimating heat flux values and liquid/vapor fractions in the predominantly liquid/vapor lines are discussed in Pandya (2023b). The uncertainties $U_{q''_w} \cong \left(\frac{1}{A_{bs}}\right)\left[\left(U_{q_{watt-meter}}\right)^2 + \left(U_{q_{leakage}}\right)^2\right]^{1/2}$ are readily estimated.

3.5.2 Driving Temperature Difference $\overline{\Delta T_D}$ and Its Error Estimate

Here the average driving temperature difference $\overline{\Delta T_D}$ [°C] is defined as

$$\overline{\Delta T_D}[°C] \equiv \bar{T}_B[°C] - T_{sat}(p_{ts})[°C]$$

where

$$\bar{T}_B \equiv \frac{1}{L_{bs}}\int_0^{L_{bs}} T_B(x).dx \tag{6}$$

The boiling surface temperature variations $T_B(x)$ over $0 \le x \le L_{bs}(5\text{ cm})$ are obtained from temperatures measured by RTDs at points B_1, B_2, and B_3 (see Fig. 6) and curve-fitting. For with-piezo subcooled cases, $T_{sat}\left(p_{ts}\right)$ is replaced by an x-dependent far-field temperature $T_{far-field}(x)$; this is discussed in Section 5.1. For such subcooled cases discussed later in this paper, $\overline{\Delta T_D} \equiv \overline{T_B(x) - T_{far-field}(x)}$. The uncertainty of $\overline{\Delta T_D}$ in Eq. (6) is given by

$$U_{\overline{\Delta T_D}}[°C] = \left[\left(U_{\bar{T}_B}\right)^2 + \left(U_{far\text{-}field(x)}\right)^2\right]^{\frac{1}{2}} \cong 0.7°C \tag{7}$$

3.5.3 Local Average HTC and Its Error Estimate

The relative uncertainty in average $\underline{HTC}$ (or $\overline{HTC}$) estimates are based on estimated uncertainty in $\bar{q}''_w$ and calculated uncertainty in ΔT_D. From the definition

$$\overline{HTC}\left[\frac{W}{cm^2 - °C}\right] \equiv \frac{\bar{q}''_w\left[\frac{W}{cm^2}\right]}{\overline{\Delta T_D}[°C]} \tag{8}$$

it follows that

$$\frac{U_{HTC}}{HTC} = \left[\left(\frac{U_{\bar{q}''_w}}{\bar{q}''_w} \right)^2 + \left(\frac{U_{\overline{\Delta T_D}}}{\overline{\Delta T_D}} \right)^2 \right]^{1/2} \tag{9}$$

Because $\overline{\Delta T_D}$ decreases for with-piezo and with-mesh cases as piezos power is increased, HTC values increase [see Eq. (8)], and therefore the uncertainty U_{HTC} [see Eq. (9) and section 5.1] also increases.

4. RESULTS

In this section, sample experimental results are reported in graphical and tabular forms for steady partial flow boiling operations over the plane and meshed boiling surfaces (with or without actuation of the piezos located outside the minichannel, as shown in Fig. 1). The estimated maximum values of uncertainties associated with data in different columns of any table are reported in the row below the column identifier headers. The sample results reported in Tables 1–4 are given for steady values of flow variables of interest and different flow-boiling scenarios. The various calculated variables of interest are described in subsections 3.5.1–3.5.3. They are calculated and reported in Tables 1–4. In addition to these variables, the following calculated variables are also assessed and discussed later in this paper.

1. CHF: The variable is discussed and its values are assessed.
2. Pumping power: Its magnitudes are assessed and discussed.
3. Resistive powers consumed by piezos: These are denoted as P_{PZ-t} values. Their calculation procedures are discussed in the appendix and reported in Section 3.4.

4.1 Basic Results

These are for partial boiling cases where the inlet liquid mass flow rate $\dot{M}_{L-in}$ in Fig. 6 exceeds the minimum mass flow rate $\dot{M}^*_{L-in} \equiv q_{bs}/h_{fg}$ that will completely vaporize it for a given heat input and it also equals the total vapor mass flow rate out of the two ports (one is a predominantly vapor

TABLE 1: Results from representative no-piezos and with-mesh cases for different heat flux $\bar{q}''_w$ values; typically $\dot{M}_{V-out} \approx \frac{1}{2}\dot{M}_{L-in}$

Test run	$\dot{M}_{L-in}$ [kg/min]	$\bar{T}_B$ [°C]	p_{ts} [kPa]	T_{sat} [°C]	$\Delta\bar{T}_D$ [°C]	$\bar{q}''_w$ [W/cm²]	$\overline{HTC}$ [W/m²°C]	$\dot{M}_{c2}$ | $\dot{M}_{c3}$ [kg/min]
	± 4.8%	± 1.3%	± 16.8%	± 16.8	± 8.9%	± 12.6%	± 15.4%	± 2.9%
1	0.041	50.1	137	45.2	4.9	8.7	17610	0.02 | 0.02
2	0.060	55.1	138	45.4	9.7	12.7	13060	0.02 | 0.04
3	0.108	61.7	129	43.6	18.1	22.1	12220	0.06 | 0.09
4	0.124	66.1	132	44.3	21.8	26.5	12150	0.05 | 0.10
5	0.161	75.7	140	45.8	29.8	35.8	11990	0.03 | 0.12
6	0.205	85.9	151	48.1	37.8	44.7	11840	0.13 | 0.14
7	0.249	100	162	50.1	50.0	53.5	10710	0.15 | 0.14
8	0.282	137	166	50.9	86.2	63.0	7310	0.17 | 0.17
9	0.321	169	175	52.4	116.7	73.1	6270	0.18 | 0.16

TABLE 2: Test section specifications for subcooled flow-boiling conditions at fixed f_M and variable piezo power P_{PZ-t} values. Subcooled because the inlet liquid temperature remains $T_{L\text{-}in} \cong 31°C$ while far-field temperature near the top of the channel increases to a higher saturation temperature by the exit (discussions in Fig. 13). Test runs are for representative with-mesh and with-piezo cases. Piezo configuration is $f_P \approx 4.869$ MHz, $|Z| = 52.4\Omega$, and $f_M = 200$ Hz. The last two columns show the total and relevant power [see appendix] consumed by piezo

Run	$\dot{M}_{L-in}$ [kg/min]	Signal input [V]	$\bar{T}_B$ [°C]	p_{ts} [kPa]	T_{sat} [°C]	$\Delta\bar{T}_D$ [°C]	$\bar{q}''_w$ [W/cm²]	$\overline{HTC}$ [W/m²°C]	$\dot{M}_{c2}$ | $\dot{M}_{c3}$ [kg/min]	P_{PZ-t} [W]	P_{PZ-R} [W]
	± 5.3%		**± 1.0%**	**± 13.1%**	**± 13.1%**	**± 20.3%**	**± 10.4%**	**± 23.1%**	**± 5.0%**	**± 1%**	**± 1%**
1	0.09	3	71.1	128	43.3	27.8	25.7	9246	0.02 | 0.08	3.11	0.391
2	0.16	4	70.5	163	50.3	23.5	25.1	10690	0.05 | 0.13	3.41	1.98
3	0.19	6	57.4	206	57.4	15.9	25.2	15880	0.06 | 0.15	3.37	2.24
4	0.18	8	66.5	303	69.6	5.2	25.3	48750	0.07 | 0.15	2.86	1.83

TABLE 3: Representative results from subcooled ($T_{L\text{-}in} \cong 31°C$) flow-boiling conditions are for with-mesh and with-piezo cases. Modulation frequency f_M varies. Signal voltage and power to the piezo are constant, at 8 Vpp and approximately 2.9 W (≤ 2.4% of the heat removal), respectively. Other piezo configurations are $f_P \approx 4.869$ MHz, and $|Z| = 52.4\Omega$

Test run	$\dot{M}_{L-in}$ [kg/min]	f_M [Hz]	$\bar{T}_B$ [°C]	p_{ts} [kPa]	T_{sat} [°C]	$\Delta\bar{T}_D$ [°C]	$\bar{q}''_w$ [W/cm²]	$\overline{HTC}$ [W/m²°C]	$\dot{M}_{c2}$ | $\dot{M}_{c3}$ [kg/min]
	± 5.3%		**± 1.0%**	**± 13.1%**	**± 13.1%**	**± 20.3%**	**± 10.4%**	**± 23.1%**	**± 5.0%**
1	0.136	1	66.9	259	64.5	9.28	24.5	26,400	0.03 | 0.14
2	0.131	100	67.6	369	76.3	5.03	24.4	48,500	0.03 | 0.14
3	0.135	200	67.2	390	78.2	6.01	24.4	40,600	0.03 | 0.14
4	0.130	300	67.8	393	78.5	5.02	24.4	48,600	0.03 | 0.14
5	0.132	400	67.5	362	75.7	6.02	24.4	40,500	0.03 | 0.14
6	0.133	500	67.4	327	72.2	5.71	24.4	42,700	0.03 | 0.14

TABLE 4: Experimental runs for other regularity-check cases involving no-piezos. Test run 1 is from a no-mesh (plane channel) and two-phase boiling configuration. Test run 2 is for a meshed test section for which a single-phase liquid flows in and out of the test section at pressures well above saturation temperatures (the vapor line is closed and there is no boiling; only liquid heating occurs). Test run 3 is from a mesh and two-phase boiling configuration. Typically, $\dot{M}_{V-out} \approx \frac{1}{2}\dot{M}_{L-in}$

Test run	$\dot{M}_{L-in}$ [kg/min]	$\bar{T}_B$ [°C]	p_{ts} [kPa]	T_{sat} [°C]	$\Delta\bar{T}_D$ [°C]	$\bar{q}''_w$ [W/cm²]	$\overline{HTC}$ [W/m² °C]	$\dot{M}_{c2} \mid \dot{M}_{c3}$ [kg/min]
	± 4.8%	± 1.3%	± 16.8%	± 16.8%	± 8.9%	± 12.6%	± 15.4%	± 2.9%
1	0.086	82.9	221	47.4	35.5	15.5	5620	0.06 | 0.03
2	0.081	76.1	204	57.0	19.1	14.9	7840	0.02 | 0.08
3	0.081	57.9	130	43.8	14.1	16.9	12020	0.02 | 0.06

exit port and the other is a predominantly liquid exit port). Thus exit vapor quality X_e gets defined as $X_e \equiv \dot{M}^*_{L-in}/\dot{M}_{L-in}$. The run cases considered in this paper have values of inlet mass flow rate $\dot{M}_{L-in}$ and heat-flux $\bar{q}''_w$ (into the test section) values that are marked by solid circles in Fig. 11. All the data points along $X_e \cong 0.53$ line in Fig. 12 have been investigated for no-piezos (meaning piezos off) and with-mesh (meaning with microstructuring) cases in Table 1.

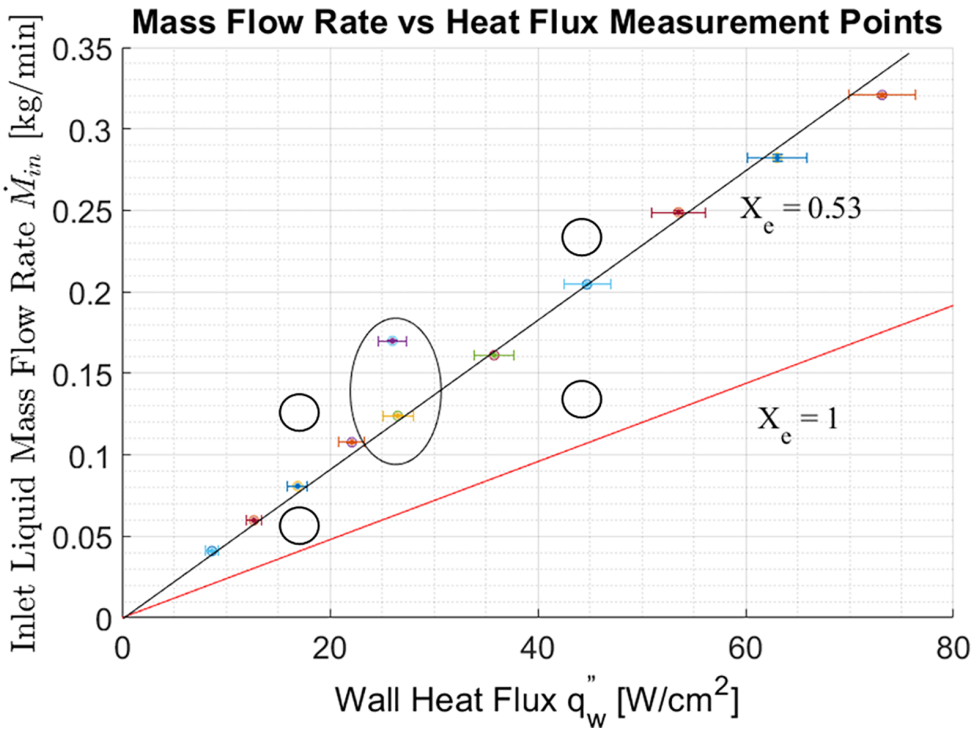

FIG. 11: To ensure partial boiling, the inlet liquid mass flow rate is always kept above (about 2 times) the minimum inlet liquid mass flow rate (the bottom line, $X_e = 1$) that corresponds to complete vaporization for a given heat flux

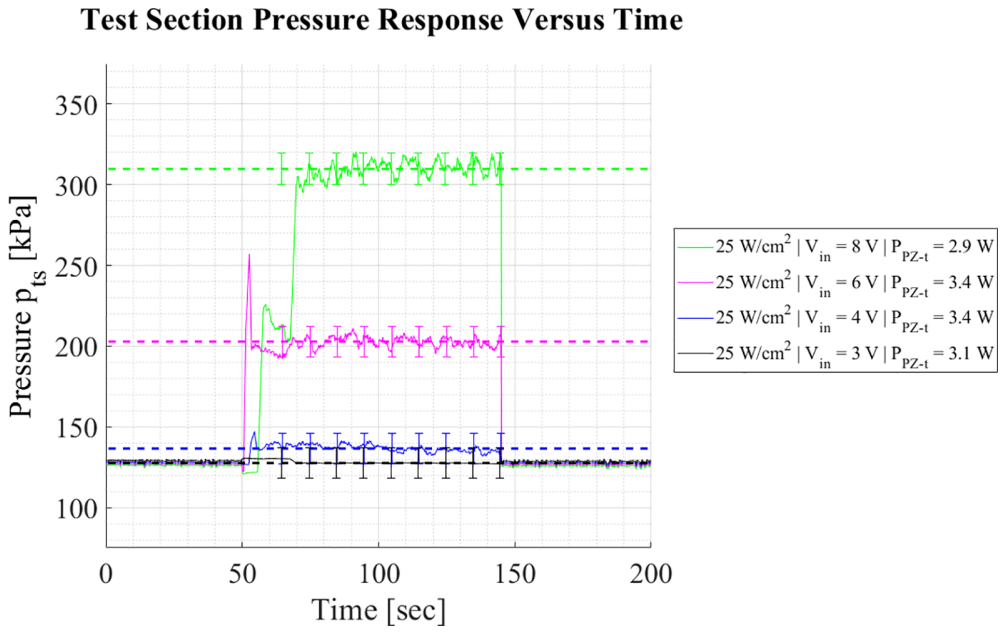

FIG. 12: The depicted test section pressure p_{ts} vs. time graphs are for cases at a heat flux of 25 W/cm^2 and modulation frequency of 200 Hz, with increasing voltage inputs V_{in} from the signal generator. Pressure rises last as long as the piezos are on

The fundamental results for with-piezo (meaning piezos on) cases, also reported many times in earlier (less well-instrumented) proof of concept (PoC) experiments (Narain et al., 2022), are shown in Fig. 12 and discussed extensively in Section 5. Here the test section pressure p_{ts} (at APT-4 location in Fig. 9) rises when the piezos are turned on with sufficient amplitude (by adjusting increases in power P_{PZ-t}) and drop back to the original value when the piezos are turned off. A sample result of this type is shown in Fig. 12. These with-piezos and with-mesh cases are reported in Table 2 (for increasing input signals' voltage or total piezo power P_{PZ-t} and fixed modulation frequency f_M) and correspond to the run cases for heat-flux $\bar{q}''_w \cong 25 \frac{W}{cm^2}$ and noted as data points in the oval zone of Fig. 11. The domain above the $X_e = 1$ in Fig. 11 has only been partially investigated. This is because $\dot{M}_{L-in} > \dot{M}^*_{L-in}$ has a second-order effect on micro nucleate building and bubble removal (and liquid filing) rates within the micro structure, which are primary contributors to the HTC values. More data points are being investigated for cases that are marked by hollow circles in Fig. 11.

There are other with-piezos and with-mesh cases discussed in Table 3 (these are for fixed total piezo power P_{PZ-t} and variable modulation frequency f_M). Table 4 presents some experimental runs for regularity checks and involves run cases involving other no-piezos cases discussed in Section 5.

The data assembled in Tables 3 and 4 are all for heat fluxes at a value of approximately 25 W/cm^2.

5. DISCUSSIONS OF KEY RESULTS

5.1 Piezo Enhanced Pressure Rise, Reductions in Driving Temperature Difference, and Significant Enhancements in HTC

For an externally imposed heat flux value of approximately 25 W/cm^2 (Fig. 12), steady test section pressure rises (p_{ts} measured by APT-4 in Fig. 9) are observed. In these runs, only one of the

pair of piezos is fired (see Fig. 1) with square-wave signal-generator signals at ultrasonic high frequencies of $f_{P1} \cong 4.87$ MHz and sonic modulation frequency of $f_{M1} \cong 200$ Hz. The rise in Fig. 12 is stronger for increasing input voltages (with associated increases in relevant piezos power P_{PZ-t} values), and the rise lasts only as long as the piezos are on (note that this kind of piezo, at these low powers, lasts years, about 40,000 to 80,000 hours of operation). Figure 12 results are similar to many others obtained by the Michigan Tech team (Narain et al., 2022). In earlier experiments and some reported here, there is a higher pressure rise when both piezos are fired (that study is not emphasized here).

The physics underlying the results in Fig. 12 is important because they show a significant drop in the driving temperature differences ΔT_D (see rows 1–4 in Table 2) and a consequent rise in boiling efficiency as measured by the significant increase in the value of the average heat transfer coefficient $(\overline{HTC})$ in Table 2. These $\overline{HTC}$ values are estimates as the with-piezos values here are for subcooled boiling, discussed below.

Since $T_{L-in} \cong T_{sat}(p_{ts}|_{NP})$ remains at saturation temperature originally associated with no-piezos test section pressure $p_{ts}|_{NP}$, the temperature $T_{far-field}(x)$ in Fig. 13 increases with distance (along the length of the boiling surface) to the higher saturation temperature associated with the higher with-piezo pressure, $p_{ts}|_{WP}$, measured at the predominantly vapor exit port of the test section (side schematic in Fig. 13).

As shown in Fig. 13, the with piezo average driving temperature difference $\Delta\overline{T}_D^{WP}$ is significantly reduced compared to the no piezo driving temperature difference $\Delta\overline{T}_D^{NP}$ $(i.e.\ \Delta\overline{T}_D^{WP} << \Delta\overline{T}_D^{NP})$. This is consistent with the values reported in Tables 1–3 for heat flux values $\cong 25$ W/cm^2 – where greater errors are also reported for significantly reduced $\Delta\overline{T}_D^{WP}$ and significantly increased with piezo HTC values.

The inlet temperature T_{L-in} can be reduced by flow control to bring the with piezo vapor exit pressure $p_{ts}|_{WP}$ and temperature $T_{sat}(p_{ts}|_{WP})$ cases back to their no piezo values in a way that allows heat flux input for the piezo cased to be reduced and values to be increased back to their no piezo cases – again

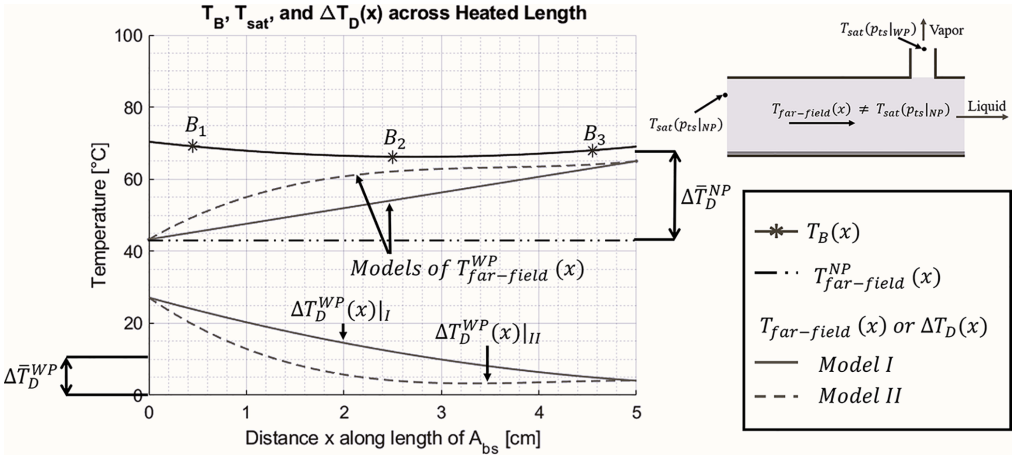

FIG. 13: Schematic shows various temperature variations with distance x (along the length of heated area A_{bs}). It shows (1) the bottom boiling temperature $T_B(x)$, (2) saturation temperatures near the inlet and the outlet that define $T_{far-field}(x)$, and (3) the driving temperature difference $\Delta T_D(x)$. Since the calculated values of driving temperature differences $\Delta T_D(x)$ are modeled by the two models with piezo (WP) cases and one model for the no piezo (NP) case, its variations along the length of the boiling surface, the estimated average driving temperature difference $\overline{\Delta T_D} \equiv T_B(x) - T_{far-field}(x)$, and the average heat transfer coefficient $\overline{HTC}$ depend on the range of estimates for $T_{far-field}(x)$.

achieving increased HTC values for the with piezo cases. But such flow controls have no practical value as most applications of interest involved fixed (or variable) externally imposed values of $\bar{q}''_w$.

In Figs. 13 and 14, the mean temperature $\overline{T_B}$ (bottom boiling surface) is computed using Eq. (6) and $T_B(x)$ variations shown in Fig. 14. Furthermore, the top two curves in Fig. 14 show that the with-piezo acoustothermal heating cases (associated with 25 W/cm^2 heat flux) lead to slightly higher temperatures $\overline{T_B}$ compared to the no-piezo cases. These are minor increases in $T_B(x)$ for with-piezo cases which are consistent with section 5.1.1 discussions for Fig. 15. The $T_B(x)$ increases are associated with small ultrasonic heating P_{PZ-t} of the microstructure as shown in Fig. 15 (which heats the large thermal inertia copper and negligible thermal inertia fluid microlayers associated with microbubbles). This P_{PZ-t} heating takes place without affecting the heat flow qbs into the bottom of the test section in Fig. 15. The significant reduction in with-piezo thermal resistance value in Fig. 15(b) is consistent with row 4 of Table 2 or rows 3–5 of Table 3 where significant lowering of $\Delta\overline{T}_D$ values occur. This leads to significant increases in $\overline{HTC} \equiv \bar{q}''_w/\Delta\overline{T}_D$ values, from around 9250 W/(m^2-°C) for no-piezo cases to around 48,000 W/(m^2-°C) for with-piezo cases.

5.1.1 Acoustothermal Heating, Mechanistic Understanding of Micronucleation within and around the Microstructured Surfaces, and the Nonequilibrium Nature of Phase-Change

Figure 15 presents a mechanistic view of the micronucleation processes for the specific microstructuring pattern (Fig. 3) used to enable the expected acoustothermal heating effects (Fig. 2) indicated for a representative point P in Fig. 3(a).

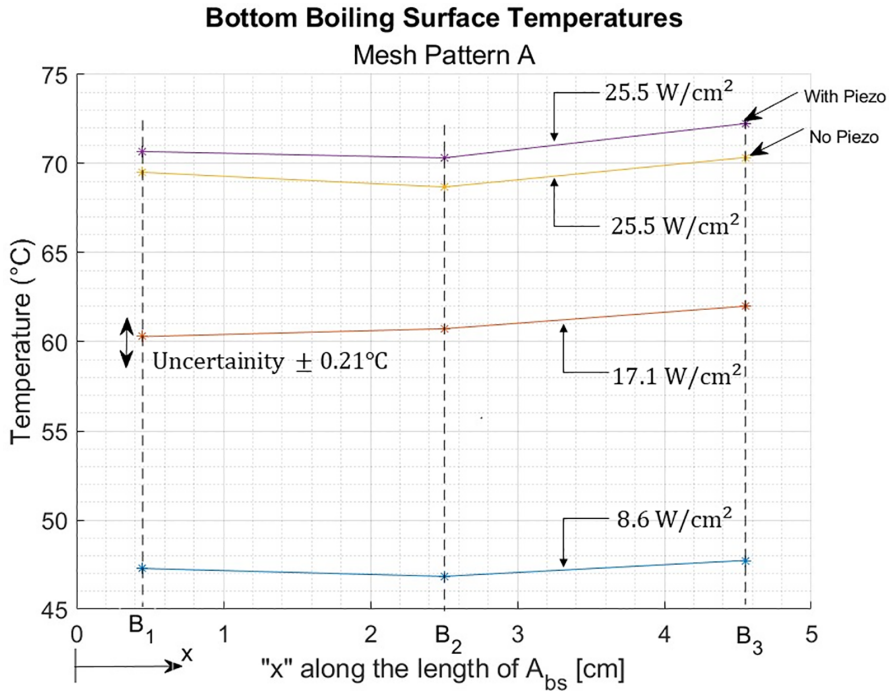

FIG. 14: Bottom boiling surface temperature variations ($T_B(x)$) are nearly uniform. This is due to the PGS sheet between the heater block and the heat sink $T_B(x)$. It increases slightly with acoustothermal heating; see the 25 W/cm^2 case.

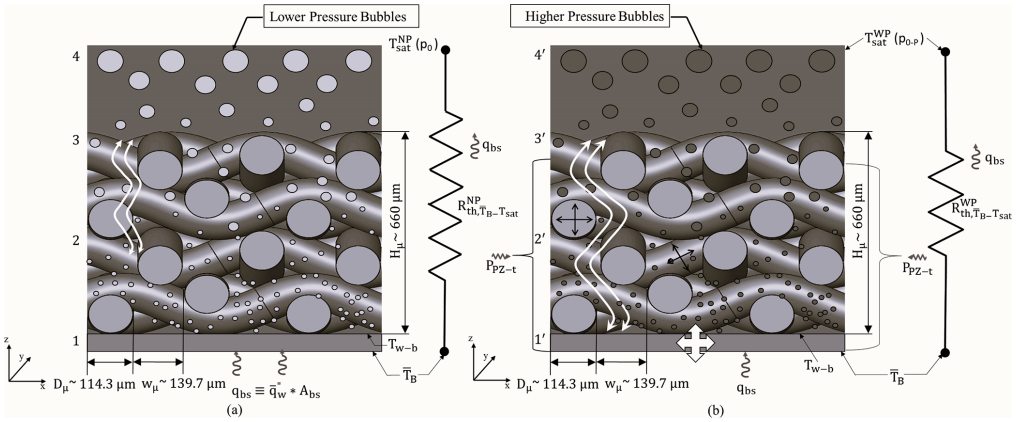

FIG. 15: (a) Passive micronucleation occurs within these types of mesh structures (based on the results of Wen et al., 2017). The bubble numbers (lower pressure bubbles) and bubble-removal/liquid-filling rates (white arrows) are self-selected and much smaller than those associated with ultrasonic-induced nonequilibrium phase change indicated in the adjacent figure. (b) Lower-pressure micro-bubbles turn into higher-pressure ones (indicated by darker bubbles) and a lot more vigorous bubble removal/liquid filling rates (indicated by the larger up and down white arrows) that are induced with the help of structural resonance associated with the imposed sonic frequencies.

As piezos at ultrasonic f_p values are turned on, they lead to additional acoustothermal heating (same phenomena as for thin film evaporation discussed in Pillai et al., 2018; Datta et al., 2021) of the microlayer (Fig. 2) associated with a microbubble nucleating at an active site near the point P in Fig. 2 (the point P relates to any nucleation-active point P in Fig. 3a). The higher evaporation rates associated with bubbles in Fig. 2(b) relative to Fig. 2(a) (the no-piezo case), lead to higher pressures within the bubble. This fact is shown in Fig. 15 by marking lower-pressure bubbles associated with no acoustothermal heating a lighter shade in Fig. 15(a) and higher-pressure bubbles arising from acoustothermal heating (i.e., after piezos are turned on) of the bubbles' microlayers a different shade/color in Fig. 15(b). Besides acoustothermal heating, the bubbles in the narrow gaps of the microstructure (despite the Wenzell filling; see Erbil and Cansoy, 2009; Murakami et al., 2014; nature of a single layer of the meshed region) in Fig. 15 require dislodging, removal through fluid emptying, and fluid refilling assistance for liquid rewetting of the pores. Some such assistance is provided for by the special gear pump arrangements (Fig. 9) for forced pushing and sucking at the special liquid inlet and outlet designed to be very close to the microstructures (blue arrows in Fig. 6). For the no-piezos case in Fig. 15(a), such fluid motion assistance is limited and indicated by smaller transverse white arrows, whereas it is more significant for with-piezos cases in Fig. 15(b). In Fig. 15(b), the bubble dislodging/ liquid refilling phenomena are aided by the much-needed fluid motion induced by the resonant structural vibrations associated with f_M (Fig. 5) where it is indicated by the larger transverse white arrows.

In Fig. 12, the much higher pressures measured for the with-piezos cases at the vapor exit port of Fig. 6 are a consequence of the much higher pressure in the dislodged bubbles of Fig. 15(b). These microbubbles exit the microstructured region, coalesce, then exit the test section, and then condense at the vapor line condensers in Fig. 9. For both no-piezos and with-piezos conditions in Figs. 6 and 15, the vapor space and vapor condensation rate ($\dot{M}^*_{L-in} \equiv q_{bs}/h_{fg} \approx \dot{M}_{c_2}$) in the condensers of Fig. 9 remain approximately the same (here vapor entrainment rates in the liquid exit port of Fig. 6 are being ignored). Under these conditions, the higher vaporization

rates associated with the with-piezos conditions of Fig. 15(b) lead to a new steadied and higher number of vapor molecules in the vapor space (for a given piezos power P_{PZ-t} at ultrasonic f_p and modulation frequency f_M), which manifests as higher pressures in Fig. 12 as long as piezos are on (i.e., the nonequilibrium phase-change thermodynamics at the interface of negligible thermal inertia heated microlayer conditions of Fig. 2b holds!). Given that the bottom boiling surface temperature $\overline{T_B}$ and the heat flux $\overline{q''_w}$ hardly change, while the driving temperature difference ΔT_D drops significantly and *HTC* increases significantly, the boiling efficiency as measured by the thermal resistance between the bottom boiling surface and the test section exit ports is significantly reduced (Fig. 15).

The results thus far require discussions on the role of the exposed surface area of the microstructure, modulation frequency f_M, piezo power P_{PZ-t}, and the transit time τ_r of the vapor between the microstructured surface in Fig. 6 and the condenser locations in Fig. 9, and the role of nonequilibrium thermodynamics for this ENB phenomena.

Furthermore, since both CHF and HTC need to be increased, CHF issues also need to be discussed (however, recent breakthroughs in the CHF increase approach are being modified in the present context and are discussed elsewhere).

5.1.2 Role of the Fluid Exposed Surface Area A_{exp} and Modulation Frequency f_M on ENB

Recall that in Section 2, the characteristic fluid-filled gap size of the microstructure (in Fig. 3) was defined as Δ_F, and in subsection 3.2.2, the fluid-exposed surface area of the microstructured region was defined as A_{exp}. An active site in Figs. 2 and 3, with or without acoustothermal heating, is one with elemental area $\delta A_{exp-active}$ where a bubble goes through its complete bubble ebullition cycle (Kunkelmann et al., 2012) of growth (with advancing and receding contact line with the substrate) followed by departure (under suitable dislodging forces) and a dwell time associated with liquid rewetting before the nucleation cycle begins again. At such sites, for bubble departure diameters in a small range of D_b to $D_b + dD_b$, there is a nonzero number of nucleating bubbles $n''(D_b)*dD_b$ per unit area of the boiling surface $\delta A_{exp-active}$ that have a frequency $f_e(D_b)$ associated with the bubble ebullition cycle. Therefore, $n''(D_b)* f_e(D_b)$ represents a spectral density function for the number of bubbles/sec/$\delta A_{exp-active}(cm^2)$ per μm/mm bubble-diameter difference dD_b in a way that $n''(D_b) * f_e(D_b * dD_b$ represents number of bubbles/sec/$\delta A_{exp-active}(cm^2)$ for bubble departure diameters in the range of D_b to $D_b + dD_b$. It is reasonable to assume here that the order of magnitude of a sufficiently small $\delta A_{exp-active}$ can be defined as

$$O(\delta A_{exp-active}) \equiv \Delta^2_F, \tag{10}$$

where $n''(D_b) * f_e(D_b) \neq 0$. Since the entire fluid exposed area A_{exp} of the microstructure is quite large (e.g., $A_{exp} \cong 6.73\ m^2$, using the definitions in Figs. 3 and 6), only a fraction α—where $0 < \alpha < 1$—of A_{exp} determines the area $A_{exp-active}$ where nucleate boiling heat transfer occurs. That is, we can define

$$A_{exp-active} = \sum \{\delta A_{exp-active}\} \equiv \alpha \cdot A_{exp} \tag{11}$$

The area $A_{exp-active}$ or fraction α in Eq. (11) is significantly dependent on whether the piezos are on or off; and when they are on, α becomes larger depending on the value of structural resonant frequency f_M and associated energy, which controls the fluid filling and bubble ejection phenomena (indicated by the size of the white up and down arrows in Fig. 15) through resonant structural vibrations of suitable mode shapes.

Furthermore, at any point P in Figs. 2 and 3, the local nucleation heat flux q''_P relates to the total nucleation heat removal rate, $q_{Nucleation-HT}$ through the relationship

$$\begin{aligned} q_{Nucleation-HT} &= \sum \{q''_P \delta A_{exp-active}\} \\ &= \int_{A_{exp-active}} q''_P \cdot dA_{exp-active} \end{aligned} \tag{12}$$

Modeling departing nucleating bubbles as spheres of diameter D_b, the vaporized mass per bubble is $\{\rho_v \cdot (\pi D_b^3)/6\}$, where ρ_v is the vapor phase density. The heat removed per bubble is $(\pi D_b^3)/6 * \rho_v * h_{fg}$, where h_{fg} is the latent heat of vaporization (J/kg in SI). With $n''(D_b)) * f_e(D_b * dD_b$ representing number of bubbles/s/$\delta A_{exp-active}\left(cm^2_{"}\right)$ for bubble departure diameters in the range of D_b to $D_b + dD_b$, the local nucleation heat-flux q''_P is given by

$$q''_P \equiv \int_0^{\infty(\text{or } \Delta_F)} n''(D_b).\left\{\left(\frac{\pi D_b^3}{6}\right).\rho_v\right\} h_{fg}.f_e(D_b).dD_b \tag{13}$$

Since all the bubble diameter D_b values are typically less than the characteristic liquid film thickness Δ_F, for order of magnitude estimates, the ∞ in the upper integral limit of Eq. (13) can be replaced by the distance Δ_F.

Substituting Eq. (13) in Eq. (12), we use the double integrals to define suitable average values of different variables and restate it as

$$q_{Nucleation-HT} \cong \left[n''_{av}(D_b^*) * \Delta_F\right]\left\{\left(\frac{\pi D_b^3}{6}\right).\rho_v\right\} h_{fg}.f_{av}(D_b^*) * A_{exp-active} \tag{14}$$

where D_b^* is an average bubble departure diameter such that $\left[n''_{av}(D_b^*) * \Delta_F * f_{av}(D_b^*)\right]$ represents number of bubbles/sec/cm^2 of the active nucleation-exposed area $A_{exp-active}$.

As an approximation, since the total heat transfer rate into the heat sink $q_{bs} \equiv \overline{q''_w} \equiv A_{bs} \cong q_{Nucleation-HT}$ remains the same in Eq. (14) for both no-piezo and with-piezo cases, it is only the active areas $A_{exp-active}$, spectral densities of bubble frequencies $f_e(D_b)$, and nucleation site densities $n''(D_b)$ that change in Eqs. (12)–(14) to accommodate higher microlayer temperatures relative to the bubble's interior vapor temperature and higher interior bubble pressures associated with acoustothermal heating cases depicted in Fig. 15(b).

5.1.3 Structural Vibration at Sonic Frequencies f_M and Its Impact on HTC Values

The fluid filling and emptying role of the modulation frequency f_M, as discussed in subsection 5.1.1 and Fig. 15, also has a direct impact on the HTC values (see Table 3) for with-piezos cases. A representative Table 3 type result for different frequencies f_M in Figs. 16 and 17 for heat flux $\overline{q''_w} \cong 25 \frac{W}{cm^2}$ demonstrates its importance. The structural vibration of Fig. 5 is only one of several factors. The fluid gap topology of Fig. 3(b), quality and stability of diffusion bonding of layers, and inlet/outlet arrangements for fluid pushing and suction from gear pumps are some of the other important factors and are part of ongoing research. The starred dots (for the single piezo cases) in Fig. 16 show that for $50 \text{ Hz} \le f_M \le 1000$ Hz, the variation with f_M is nonmonotone and the value $f_M = 200$ Hz has the best structural vibrations mode-shape for, perhaps, resonant interactions with the micro bubbles ebullition cycles (via Bjerknes forces discussed in Douglas et al., 2012) leading to the highest HTC. Figure 17 plots another Fig. 16 type of result for a different

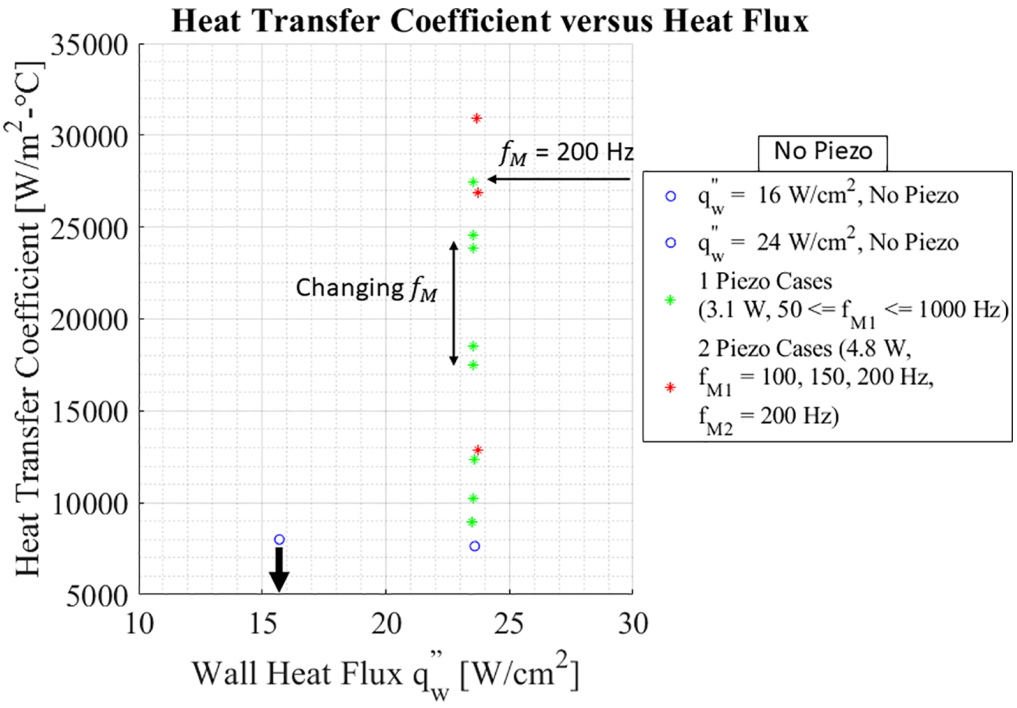

FIG. 16: Results for heat flux $\bar{q}''_w \cong 24$ W/cm^2, with varying f_M. This is from a set of runs that are not indicated in Table 3.

and higher P_{PZ-t} piezo power case with a range of modulation frequencies 150 Hz $\le f_M \le$ 450 Hz, which yields higher HTC values. These results show the possibility of optimizing HTC and ε_T (see Eq. 1) values by smart (possibly machine-learning–based) choices of modulation frequency f_M and piezo power P_{PZ-t}.

In Fig. 16, for $\bar{q}''_w \cong 18 \frac{W}{cm^2}$, experimentally obtained HTC values are obtained for several regularity check cases in Table 4, and the order of magnitude of these values are consistent with various known correlations compiled by other researchers (Carey et al., 2018; Narain et al., 2018; Gungor and Winterton, 1986).

5.1.4 Impact of Substructural Vibrations Amplitudes on HTC

The HTC versus input signal voltage results of Table 2 are plotted in Fig. 18. The results clearly show increasing HTC with increasing power of the ultrasonic vibrations for a fixed modulation frequency. The microstructure stability issues discussed in Fig. A.1 of the Appendix deal with other relevant issues concerning better monotonicity of P_{PZ-t} and P_{PZ-R} relations expected in forthcoming experimental runs.

5.1.5 Another Role of Modulation Frequency f_M and Transit Time τ_r on ENB

The nearly stagnant fluid and bubbles in the narrow gaps of the microstructure (despite the Wenzell filling nature of a single layer of the meshed region; Erbil and Cansoy, 2009; Murakami et al., 2014) require emptying and filling assistance from this much-needed motion induced by structural vibrations associated with f_M, as well as from the special gear pump arrangements for

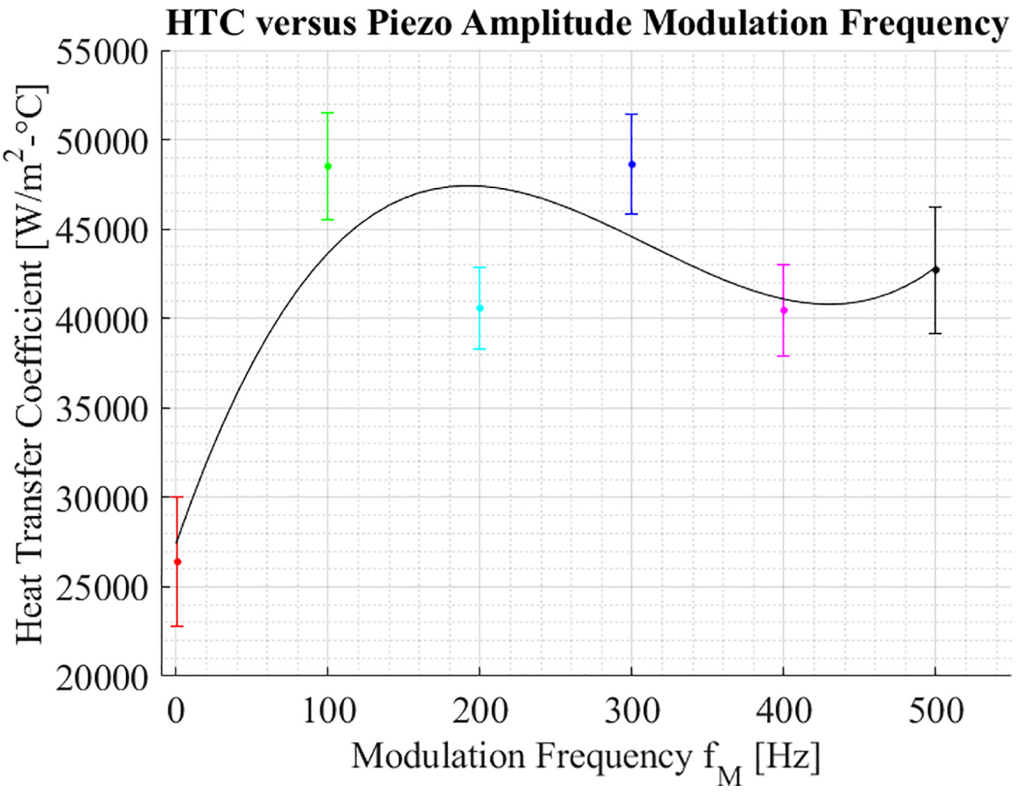

FIG. 17: Heat transfer coefficient over a range of different modulation frequencies. Modulation frequencies within the 100 to 300 Hz range result in the highest HTC values. These runs are indicated in Table 3.

forced pushing and sucking at the liquid inlet and outlet (blue arrows in Fig. 6). It is expected that the acoustothermal heating is limited to microlayers occupying a small substrate area $A_{exp-active}$ in Eq. (11) and therefore have small thermal inertia. As a result, when piezos are switched off, the loss of pressure rise in Fig. 12 appears almost immediately. This points to a nonequilibrium phase change; the steady-in-the-mean pressure rise in Fig. 12 when piezos are on is most likely a line with pixels rather than a continuous analog signal. This is confirmed by what is observed when the off period for the ultrasonic frequency is long (e.g., for $f_M \leq 1$ Hz, the off period of the square wave modulation is ≥ 0.5 s), as seen in results plotted in Fig. 19. Figure 19 shows pressure spikes with a gradual rise time and gradual fall time (termed vapor transit or pressure relaxation time $\tau_r = 0.2$ sec), followed by a quiescent period of 0.3 sec (equal to $\frac{1}{2f_M} - \tau_r$). Here, $\tau_r = 0.2$ sec is the time it takes, after 0.5 s of increases in the number of vapor molecules inside of the bubbles and consequent increases in pressures (in the available vapor domains) due to prior acoustothermal heating of the bubbles' microlayers, for number of vapor molecules to go back to the original number and recover the pressure values associated with the absence of ultrasonic excitations. This is the time it takes for the microbubbles to dislodge, merge, coalesce, leave the test section, and condense those extra molecules at the liquid/vapor interfaces of the vapor line condensers in Fig. 9. It is assumed that, in much less time than this, the low thermal inertia microlayers cool back to the original temperatures. This recovered pressure associated with the original no-piezo test section pressures stays for $\frac{1}{2f_M} - \tau_r \cong 0.3$ s before ultrasonic heating begins all over again. Clearly, steady-in-the-mean pressure rises are seen in Fig. 12 because of this periodic pressure

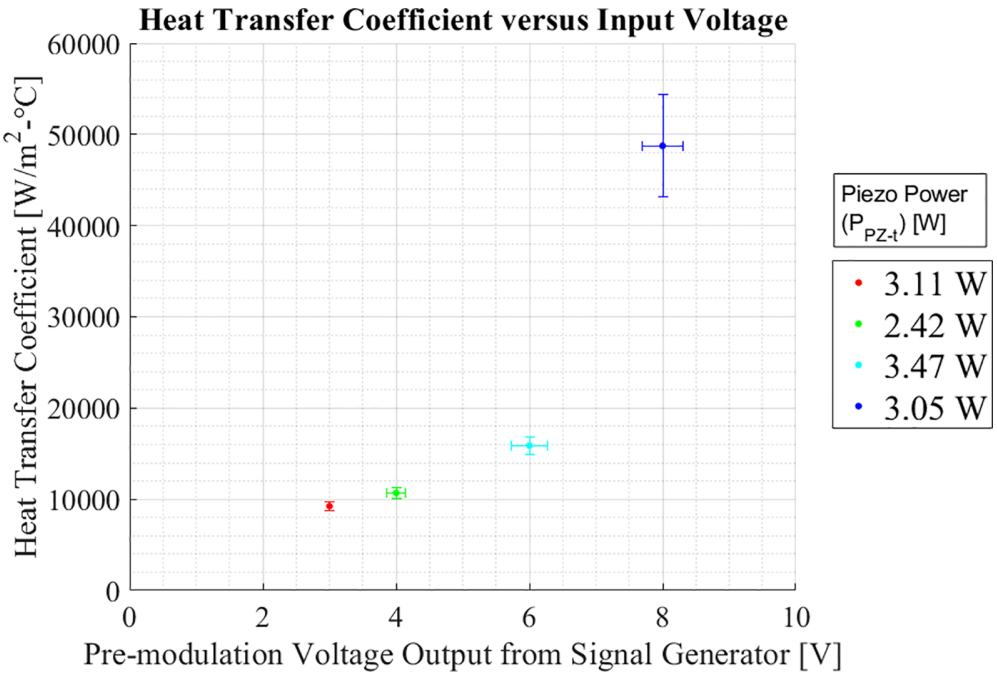

FIG. 18: Impact of pressure-rise on HTC. The result for heat flux $\bar{q}''_w \cong 24$ W/cm^2 is shown here as a function of piezo-1's power P_{PZ-t}. Here $f_M = 200$ Hz.

spikes phenomenon is absent for $f_M \geq 100$ Hz in Fig. 12. In all these cases of Fig. 12, the off time of 0.005 sec or less is much smaller than the vapor transit pressure time (same as vapor pressure relaxation time) of 0.2 sec.

As described above, nonequilibrium phase-change involving heterogeneous nucleation is not uncommon (see Avedisian et al., 2018 and other literature on flash boiling); what is likely unique about the phenomena described above is its possible controllable nature across the length and time scales (nm/μm for length and sub μs for time at the lower end) to the macroscale (> mm and > 0.2 s).

The test-section pressure p_{ts} is measured in the far field well above the mesh and into the mostly vapor exit region of Fig. 6. Here the temperature is experimentally found to be nearly equal to the saturation temperature $T_{sat}(p)$ corresponding to the measured pressure $p = p_0$ or $p = p_{0-p}$. This fact is depicted by curves 1-2-3-4, marked in Fig. 20(a), which correspond to average (at a given y) fluid temperature variations $T_{L/V}(y)$ in Fig. 20(b) as well as corresponding physical location in Fig. 15(a) as we go along the vertical distance $y \geq 0$. The conditions for $y \geq H_\mu$ in Fig. 15(b), where H_μ is typically the order of magnitude of the mesh height, correspond to equilibrium phase-change conditions above the microstructures. For no-piezos cases involving thermally nucleating microbubbles, we typically operate in the metastable region's point 1 in Fig. 20(a). This corresponds with operations at the bottom of the mesh where the temperature is the superheated bottom wall temperature T_{w-b} [Fig. 20(b)]. As we move along points 1 to 4 in Fig. 20(a), we traverse the standard thermal boundary layer (solid curve) in Fig. 20(b) and start operating under local equilibrium thermodynamic conditions for $y \geq y_3 > H_\mu$ locations well above the meshed regions. When acoustothermal ultrasonic heating of the microlayers begins for micro bubbles within the microstructure, the same metastable point 1 has a new thermodynamic condition denoted by 1′ at the bottom of the microstructure [see Fig. 20(b)] and this is in

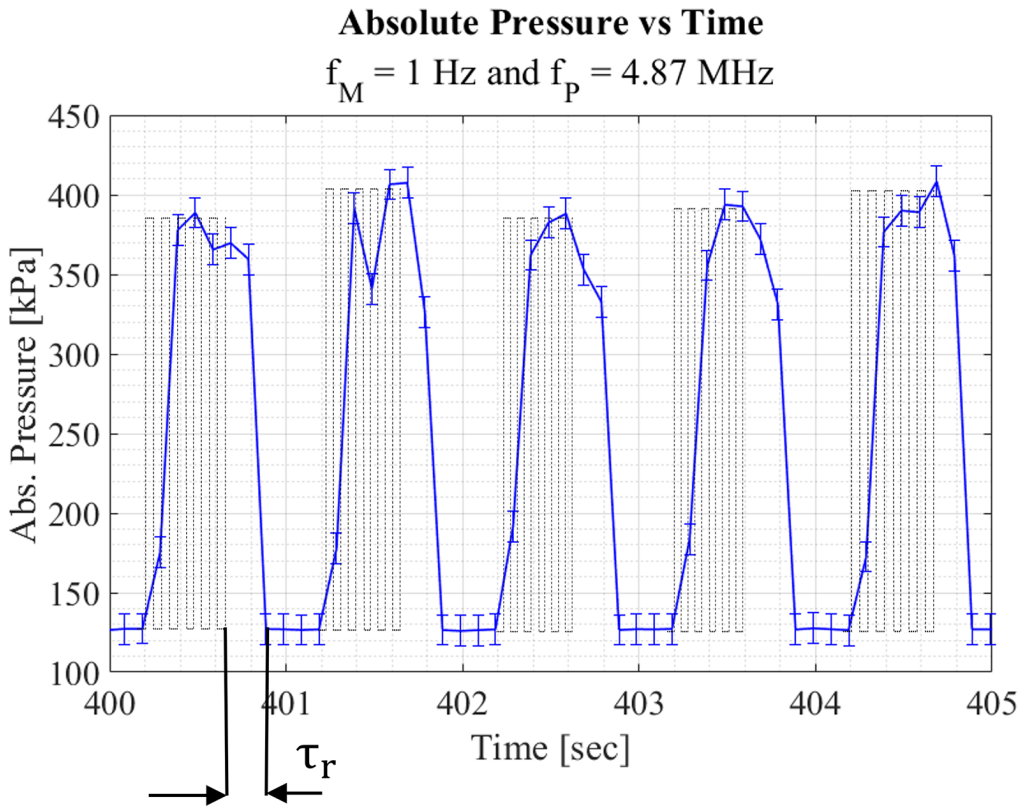

FIG. 19: The above test section pressure versus time curve is for $\bar{q}''_w \cong 25$ W/cm^2, $f_P = 4.87$ MHz, and $f_M = 1$ Hz. Only one piezo at P_{PZ-t} is operational. The result gives an understanding of why sustained piezo excitations f_p are no longer steady. (a) The relaxation time $\tau_r \cong 0.2$ sec < 0.5 sec of the off time; it is the time it takes when ultrasonic excitations (in the vertically shaded zone) are stopped to the time when the test section pressure p_{ts} is back to the no-piezos levels.

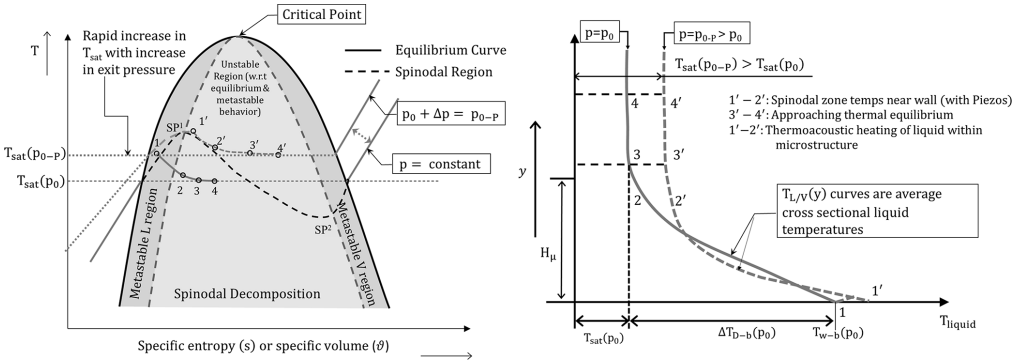

FIG. 20: (a) Equilibrium metastable and spinodal decomposition boundaries in temperature T versus specific volume v (or specific entropy s) plane. (b) Fluid phase thermal boundary layer profiles for no-piezos and with-piezos cases within the mesh pores.

the unstable spinodal decomposition region of Fig. 20(a). The fact that this condition is unstable (and corresponds to being in the evaporation regime-1 of Pillai et al., 2018) is supported by the observation that if ultrasonic heating is stopped for long (as for $f_M \leq 1$) or altogether, the with-piezo elevated pressures $p_{0\text{-}P} = p_0 + \Delta p$ [Fig. 20(a)] is not sustained (or achieved in the absence of the modulation frequency f_M in Fig. 1c). And yet, if we go far above the mesh [$y \geq H_\mu$ in Fig. 20(b)] and if flow control over time is such that we retain the original inlet pressures p_0 and saturation temperature $T_{sat}(p_0)$ at the inlet of the test section in Fig. 6, as we transverse vertical distance above the microstructure feeding into the vapor exit along the curve 1′-2′-3′-4′in Fig. 20(b) which also corresponds to the similarly labeled physical locations in Fig. 15(b), a different equilibrium saturation condition is attained by the predominantly vapor exit (where a higher test section pressure $p_{ts} = p_{0\text{–}P}$ is achieved). This subcooled boiling leads to higher HTC than the no-piezos cases (as discussed in Fig. 13 for its far-field temperature models). This is consistent with what is seen in Fig. 12 and Table 2.

By using a combination of flow control, different cooling rates in the vapor line condensers, and control of the liquid inlet temperatures at the test section (Fig. 6) inlet, a range of high pressures and saturation temperatures in the vapor phase of Fig. 20(a) and with-piezo bottom boiling surface temperature $\overline{T_B}$ in Fig. 14 may be possible provided heat flux into the test section is suitably varied (and these high HTC realizations will correspond to a range of saturated to subcooled partial flow-boiling conditions in Figs. 6 and 13).

5.2 HTC versus Heat Flux and CHF Values

In this paper, CHF studies are limited to no-piezos cases in Table 1. Graphical representation of heat flux $\overline{q}''_w$ versus driving temperature difference ΔT_D are plotted in Figs. 21 and 22, and HTC versus ΔT_D values in Fig. 23. From these, it is concluded that $\overline{q}''_{CHF} \cong 60 \frac{W}{cm^2}$.

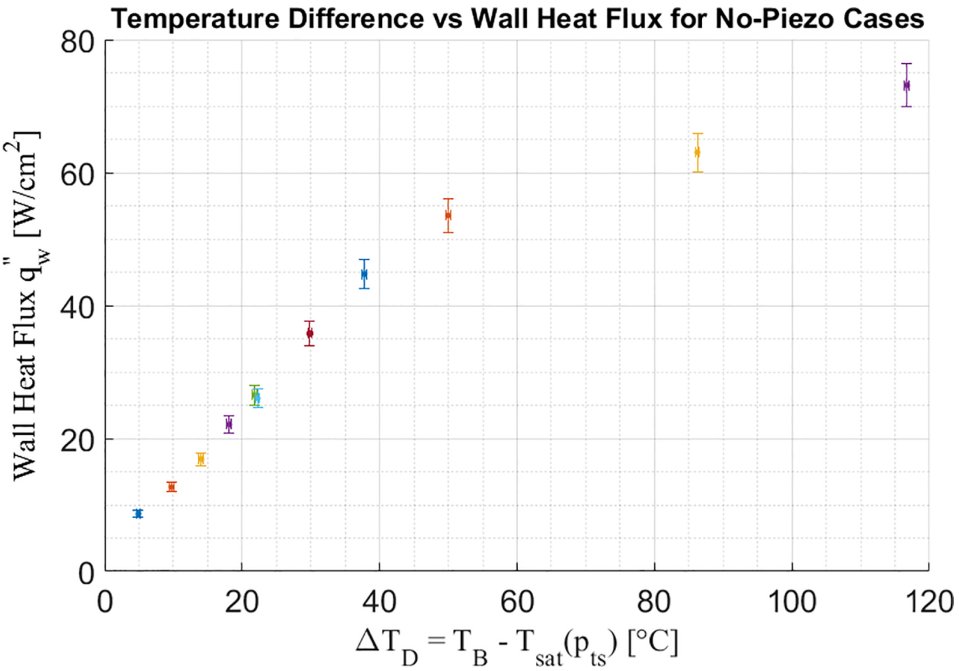

FIG. 21: Driving temperature differences start increasing exponentially around a $\overline{q}''_{CHF} \approx 60$ W/cm^2

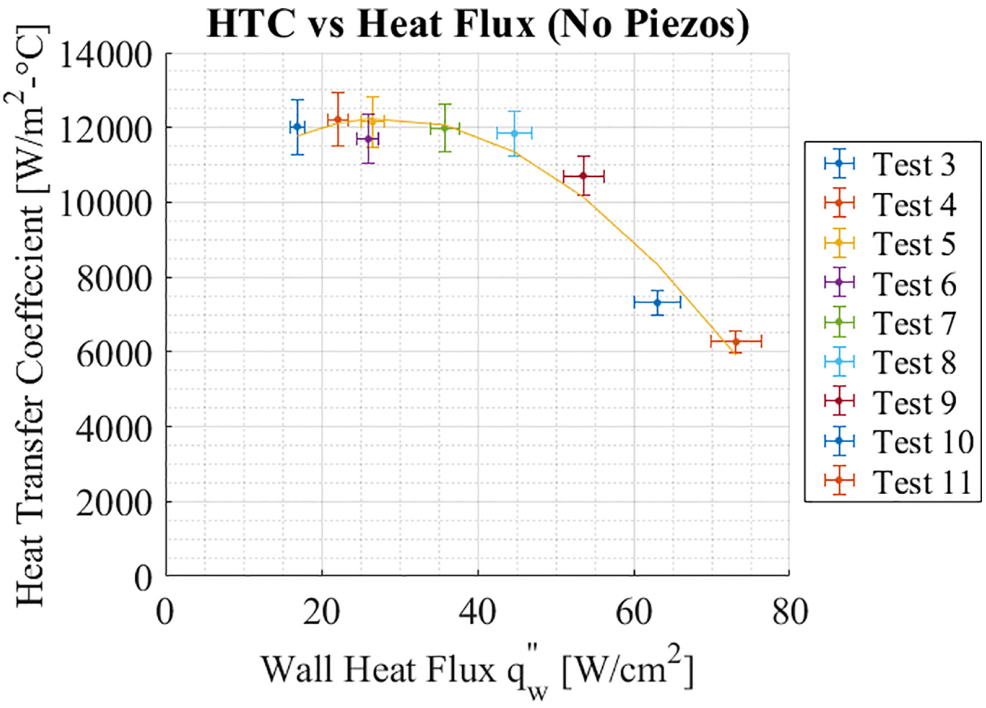

FIG. 22: HTC values start dropping around a $\bar{q}''_{CHF} \approx 60$ W/cm^2

The result in Fig. 23 for $\bar{q}''_w \cong 60$ W/cm^2 shows the onset of unsteadiness concerning bottom wall temperatures. This establishes the onset of CHF instabilities (Carey et al., 2018; Faghri and Zhang, 2006). As an estimate, for now, CHF for the with-piezo cases can also be considered to be around $60 \frac{W}{cm^2}$.

5.2.1 Further CHF Discussions

Through the understanding gained and reported above, there are changes in microstructuring patterns, test section configurations for liquid rewetting, and superior liquid pushing arrangements (using the two gear pumps) that are currently being implemented for a pool boiling type arrangement. There are additional test section changes that will ensure sustained liquid rewetting of the microstructure. These new results, being reported elsewhere, are likely to establish $\bar{q}''_{CHF} \geq 200 \frac{W}{cm^2}$.

5.3 Related Forthcoming Works Being Reported Elsewhere

With or without the help of hardware changes discussed in subsection 5.2.1, for brevity, the following other completed and ongoing works are being reported elsewhere:

- Additional experimental runs
- Nondimensional range of parameters considered and nondimensional plots of the results reported in this paper
- Complete discussions of how system-level start-up, inventory, and flow control are essential for reaching a steady state in a short duration of time while avoiding and suppressing system-level instabilities discussed in Section 1

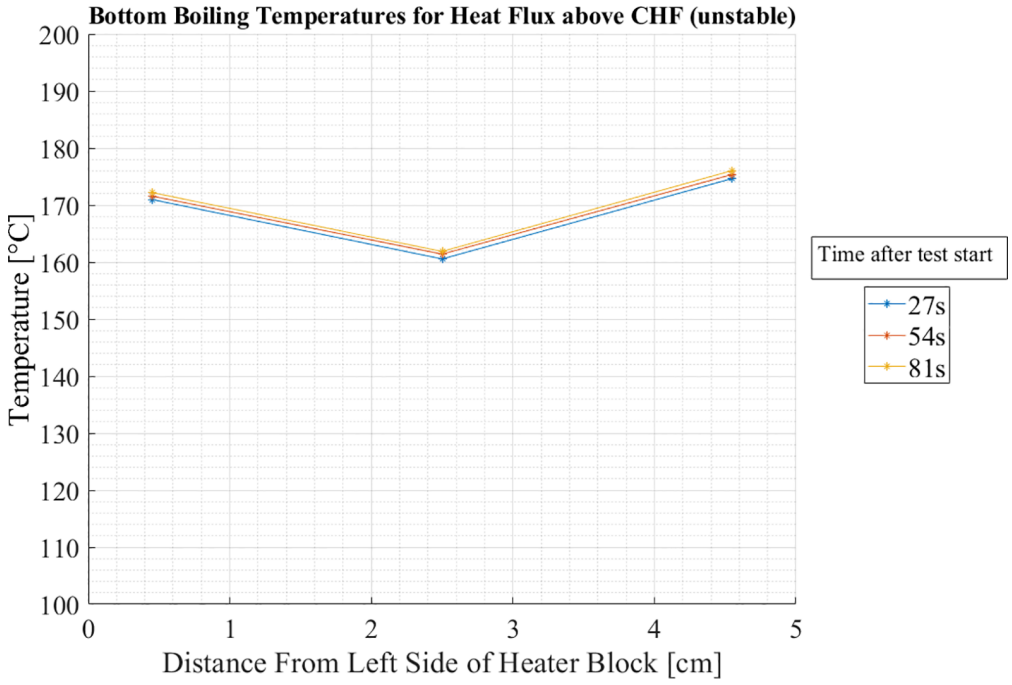

FIG. 23: The bottom boiling surface temperatures start becoming unsteady (and rising) around the $\overline{q}''_{CHF} \approx 60$ W/cm^2

- Calculated values of low pumping powers needed for the test section (< 2 W for the earlier data range covered in this paper) in support of subsection 3.2.1
- Estimates on bubbling frequencies and pressure rise phenomena for with-piezo cases based on power-spectral-density function analysis of APT-1 and APT-4 at a data acquisition rate of 3000 Hz
- Results for other more stable microstructures
- Attainment of total piezos power consumption P_{PZ-t} to values less than 1% of the total heat removed, at heat fluxes up to the new significantly enhanced CHF values

6. CONCLUSIONS

A new enhanced micronucleation approach for flow boiling (of Novec 3M Engineering Fluids) over a heated fluid-filled micromeshed region of a copper minichannel is reported. The approach utilizes additional phase-change through ultrasonic vibrations-induced acoustothermal (Pillai et al., 2018; Datta et al., 2021) heating of within mesh liquid microlayers that exist between the copper mesh and the thermally nucleated microbubbles. In addition, there is a new approach for enhancing departure rates of nucleating bubbles within the fluid-filled and heated mesh pores. This is achieved through the introduction of sonic modulation frequencies that lead to resonant structural vibrations of the microstructure and enhance fluid filling and emptying motions within the microstructure. The convective fluid motion above the micro structure plays a role in moving the heat carrying vapor bubbles out of the test section, but plays a minor role in impacting the HTC values (as ascertained here).

As a result of these processes, significantly increased HTC values (~50,000 W/m^2–°C for heat-flux of about 30 W/cm^2) are achieved. This follows from a significant reduction in driving

temperature differences (between the heated surface and saturation temperature). Ongoing investigations are also addressing thermal packaging and CHF enhancement issues. For example, the use of the latest thermal interface materials, TIM) can reduce the temperature difference between the heat source (chip or heaters) and the heatsink's bottom wall as well as microvibrations reaching the chip.

Internal and external instabilities have been delayed for the heat sink. Internal ones can be further delayed by achieving increased CHF values by enhanced liquid wetting resulting from test section modifications. These works are expected to reduce piezos' power consumption to less than 1% of the heat removal rates and heat fluxes reaching new increased CHF values (from the currently estimated levels of 60–80 W/cm^2 to values greater than 150 W/cm^2). External system-level flow instabilities are suppressed and delayed through the use of specialized hardware and flow control. The use of approximate phase separation (by the test-section exit), enabled by this flow loop, reduces test-section pumping power (Pandya, 2023b) to less than 2 W for the data reported here. The flow loop and flow control reported here can enable a new automated machine-learning–based flow control.

ACKNOWLEDGMENTS

We acknowledge seed funding from private gifts received through the Michigan Tech Fund and from NSF-CBET-2327965. Also, for improved descriptions of the microstructuring geometry, we acknowledge help received from MTU's Nucor Lab (microscope) as well as Jeremy Esch, Dr. Paul Fraley, and Dr. Daniel Sequin. We also thank Jeff Zahnd, CTO, APC, Inc., for providing the piezos and helping arrange integrations with Yektasonics piezo drivers.

REFERENCES

3M™ Novec™ 7000 Engineered Fluid Product Information, accessed October 19, 2022, from https://multimedia.3m.com/mws/media/199818O/3m-novec-7000-engineered-fluid.pdf, 2022.

APC International, Ltd., *Piezoelectric Ceramics: Principles and Applications*, APC International, 2002.

Avedisian, C.T., Skyllingstad, K., Cavicchi, R.C., Lippe, C., and Carrier, M.J., Initiation of Flash Boiling of Multicomponent Miscible Mixtures with Application to Transportation Fuels and Their Surrogates, *Energy Fuels*, vol. **32**, no. 9, pp. 9971–9981, 2018.

Bhatt, B.L. and Wedekind, G.L., A Self-Sustained Oscillatory Flow Phenomenon in Two-Phase Condensing Flow Systems, *ASME J. Heat Transf.*, vol. **102**, no. 4, pp. 694–700, 1980.

Boziuk, T.R., Smith, M.K., and Glezer, A., Enhanced Boiling Heat Transfer on Plain and Featured Surfaces Using Acoustic Actuation, *Int. J. Heat Mass Transf.*, vol. **108**, pp. 181–190, 2017.

Bigham, S. and Saeed, M., Microscale Study of Mechanisms of Heat Transfer during Flow Boiling in a Microchannel, *Int. J. Heat Mass Transf.*, vol. **88**, pp. 111–121, 2015.

Carey, V.P., *Liquid Vapor Phase Change Phenomena: An Introduction to the Thermophysics of Vaporization and Condensation Processes in Heat Transfer Equipment*, Boca Raton, FL: CRC Press, 2018.

Cheesewright, R., Clark, C., and Bisset, D., The Identification of External Factors which Influence the Calibration of Coriolis Mass Flow Meters, *Flow Meas. Instrum.*, vol. **11**, no. 1, 2000.

Chen, H. and Jebson, R.S., Factors Affecting Heat Transfer in Falling Film Evaporators, *Food Bioprod. Process.*, vol. **75**, no. 2, 1997.

Chen, J.C., Correlation for Boiling Heat Transfer to Saturated Fluids in Convective Flow, *Ind. Eng. Chem. Process.*, vol. **5**, no. 3, 1966.

Chiapero, E.M., Fernandino, M., and Dorao, C.A., Review on Pressure Drop Oscillations in Boiling Systems, *Nucl. Eng. Des.*, vol. **250**, 2012.

Chu, K.H., Joung, Y.S., Enright, R., Buie, C.R., and Wang, E.N., Hierarchically Structured Surfaces for Boiling Critical Heat Flux Enhancement, *Appl. Phys. Lett.*, vol. **102**, no. 15, 2013.

Coleman, H.W., Steele, J., and Glenn, W., *Experimentation and Uncertainty Analysis for Engineers*, New York: Wiley, 1999.

Datta, S., Pillai, R., Borg, M.K., and Sefiane, K., Acoustothermal Nucleation of Surface Nanobubbles, *Nano Lett.*, vol. **21**, no. 3, pp. 1267–1273, 2021.

DCLC & D2C Liquid Cooling Technology Vendors, CoolIT, Asetek, and Atos, from https://www.asetek.com and https://atos.net/en/solutions/high-performance-computing-hpc, (n.d.).

Douglas, Z., Boziuk, T.R., Smith, M.K., and Glezer, A., Acoustically Enhanced Boiling Heat Transfer, *Phys. Fluids*, vol. **24,** no. 5, 2012.

Erbil, H.Y. and Cansoy, C.E., Range of Applicability of Wenzel and Cassie – Baxter Equations for Superhydrophobic Surfaces, *Langmuir*, vol. **25**, no. 24, pp. 14135–14145, 2009.

Faghri, A. and Zhang, Y., *Transport Phenomena in Multiphase Systems*, Elsevier, 2006.

Gungor, K.E. and Winterton, R.H.S., A General Correlation for Flow Boiling in Tubes and Annuli, *Int. J. Heat Mass Transf.*, vol. **29**, no. 3, pp. 351–358, 1986.

Heffington, S. and Glezer, A., Enhanced Boiling Heat Transfer by Submerged Ultrasonic Vibrations, *Proc. of the Therminic*, 2004.

Hewitt, G.F., Critical Heat Flux in Flow Boiling, in *International Heat Transfer Conference Digital Library*, New York: Begell House Inc., 1978.

Kakac, S. and Bon, B., A Review of Two-Phase Flow Dynamic Instabilities in Tube Boiling Systems, *Int. J. Heat Mass Transf.*, vol. **51**, nos. 3–4, pp. 399–433, 2008.

Kandlikar, S.G., A General Correlation for Saturated Two-Phase Flow Boiling Heat Transfer inside Horizontal and Vertical Tubes, *J. Heat Transf.*, vol. **112**, no. 1, pp. 219–228, 1990.

Kenning, D.B.R. and Cooper, M.G., Saturated Flow Boiling of Water in Vertical Tubes, *Int. J. Heat Mass Transf.*, vol. **32**, no. 3, pp. 445–458, 1989.

Kim, J., Review of Nucleate Pool Boiling Bubble Heat Transfer Mechanisms, *Int. J. Multiph. Flow*, vol. **35**, no. 12, pp. 1067–1076, 2009.

Kim, S.-M. and Mudawar, I., Universal Approach to Predicting Two-Phase Frictional Pressure Drop for Mini/Micro-Channel Saturated Flow Boiling, *Int. J. Heat Mass Transf.*, vol. **58**, nos. 1–2, pp. 718–734, 2013.

Kunkelmann, C., Ibrahem, K., Schweizer, N., Herbert, S., Stephan, P., and Gambaryan-Roisman, T., The Effect of Three-Phase Contact Line Speed on Local Evaporative Heat Transfer: Experimental and Numerical Investigations, *Int. J. Heat Mass Transf.*, vol. **55**, nos. 7–8, pp. 1896–1904, 2012.

Lee, J. and Mudawar, I., Two-Phase Flow in High-Heat-Flux Micro-Channel Heat Sink for Refrigeration Cooling Applications: Part I—Pressure Drop Characteristics, *Int. J. Heat Mass Transf.*, vol. **48**, no. 5, pp. 928–940, 2005.

Liu, D., Li, Y., and Hu, A., Visualization of Boiling Heat Transfer on Copper Surface with Different Wettability, *J. Therm. Sci.*, vol. **31**, no. 6, pp. 1903–1913, 2022.

Maulbetsch, J.S. and Griffith, P., *System-Induced Instabilities in Forced Convection Flows with Subcooled Boiling,* International Heat Transfer Conference Digital Library, 1966.

Moffat, R.J., Using Uncertainty Analysis in the Planning of an Experiment, *J. Fluids Eng.*, vol. **107**, no. 2, pp. 173–178, 1985.

Murakami, D., Jinnai, H., and Takahara, A., Wetting Transition from the Cassie–Baxter State to the Wenzel State on Textured Polymer Surfaces, *Langmuir*, vol. **30**, no. 8, pp. 2061–2067, 2014.

Narain, A., Pandya, D., Agata, N., Vivek, V., Sepahyar, S., and Jaolekar, C., *A Combined Active (Piezos) and Passive (Microstructuring) Enhanced Micro-Nucleation Rate Flow-Boiling Approach for Stable High Heat-Flux Cooling*, New York: Begell House Inc., 2023.

Narain, A., Ranga Prasad, H., and Koca, A., Internal Annular Flow-Boiling and Flow-Condensation: Context, Results, and Recommendations, in *Handbook of Thermal Science and Engineering*, vol. **3**, pp. 1–88, 2018.

Narain, A., Sepahyar, S., Pandya, D., and Vivek, V., Nucleation Control System and Method Leading to Enhanced Boiling Based Electronic-Cooling, United States Patent US20220015266A1, filed Nov. 12, 2019, and issued Jan. 12, 2022.

Narumanchi, S., Mihalic, M., Moreno, G., and Bennion, K., Design of Light-Weight, Single-Phase Liquid-Cooled Heat Exchanger for Automotive Power Electronics, *13th InterSociety Conf. on Thermal and Thermomechan. Phenom. in Electronic Systems*, San Diego, CA, pp. 693–699, 2012.

Pandya, D., Narain, A., Sommerville, J., Agata, N., Damsteegt, J., and Loparo, S., Heat Transfer, Process, and Flow-Control Results for an Actively (Piezos) and Passively (Microstructuring) Enhanced Partial Flow-Boiling Approach for Stable High Heat-Flux Cooling with Dielectric Fluids, 2023a.

Pandya, D., Stable Energy-Efficient Macro-Scale Partial Flow-Boiling Using Microstructured Surfaces and Ultrasonics*,* PhD, Michigan Technological University, 2023b.

Peng, C., Ravi, S., Patel, V.K., Momen, A.M., and Moghaddam, S., Physics of Direct-Contact Ultrasonic Cloth Drying Process, *Energy*, vol. **125**, pp. 498–508, 2017.

Pillai, R., Borg, M.K., and Reese, J.M., Acoustothermal Atomization of Water Nanofilms, *Phys. Rev. Lett.*, vol. **121**, no. 10, p. 104502, 2018.

Qu, W. and Mudawar, I., Measurement and Correlation of Critical Heat Flux in Two-Phase Micro-Channel Heat Sinks, *Int. J. Heat Mass Transf.*, vol. **47**, nos. 10–11, pp. 2045–2059, 2004.

Qu, W. and Mudawar, I., Measurement and Prediction of Pressure Drop in Two-Phase Micro-Channel Heat Sinks, *Int. J. Heat Mass Transf.*, vol. **46**, no. 14, pp. 2737–2753, 2003.

Rangarajan, S., Schiffres, S., and Sammakia, B., A Review of Recent Developments in "On-Chip" Embedded Cooling Technologies for Heterogeneous Integrated Applications, *Engineering*, vol. **26**, pp. 185–197, 2023.

Rawlins, C., *Basic AC Circuits*, Elsevier, 2000.

Schwarz, B.J. and Richardson, M.H., Experimental Modal Analysis, *CSI Reliability Week*, vol. **35**, no. 1, pp. 1–12, 1999.

Schweikert, K., Sielaff, A., and Stephan, P., On the Transition between Contact Line Evaporation and Microlayer Evaporation during the Dewetting of a Superheated Wall*, Int. J. Therm. Sci.*, vol. **145**, p. 106025, 2019.

Shariff, Y.M., Acoustics Vibrations to Enhance Flow Boiling in Micro Channels, *Int. J. Therm. Environ. Eng.*, vol. **2**, no. 1, pp. 19–25, 2011.

Swarnkar, A. and Lakhera, V.J., Ultrasonic Augmentation in Pool Boiling Heat Transfer over External Surfaces: A Review, *Proc. of the Inst. Mechan. Eng., Part C: J. Mechan. Eng. Sci.*, vol. **235**, no. 11, pp. 2099–2111, 2021.

Tamvada, S.R., Alipanah, M., and Moghaddam, S., Membrane-Based Two-Phase Heat Sinks for High Heat Flux Electronics and Lasers, *IEEE Trans. Compon. Packaging Manuf. Technol.*, vol. **11**, no. 10, pp. 1734–1741, 2021.

Thiagarajan, S.J., Yang, R., King, C., and Narumanchi, S., Bubble Dynamics and Nucleate Pool Boiling Heat Transfer on Microporous Copper Surfaces, *Int. J. Heat Mass Transf.*, vol. **89**, pp. 1297–1315, 2015.

Waye, S.K., Narumanchi, S., Mihalic, M., Moreno, G., Bennion, K., and Jeffers, J., Advanced Liquid Cooling for a Traction Drive Inverter Using Jet Impingement and Microfinned Enhanced Surfaces, *Fourteenth Intersociety Conf. on Thermal and Thermomechan. Phenom. in Electronic Systems (ITherm)*, pp. 1064–1073, 2014.

Weisman, J. and Pei, B.S., Prediction of Critical Heat Flux in Flow Boiling at Low Qualities, *Int. J. Heat Mass Transf.*, vol. **26**, no. 10, pp. 1463–1477, 1983.

Wen, R., Li, Q., Wang, W., Latour, B., Li, C.H., Li, C., Lee, Y.-C., and Yang, R., Enhanced Bubble Nucleation and Liquid Rewetting for Highly Efficient Boiling Heat Transfer on Two-Level Hierarchical Surfaces with Patterned Copper Nanowire Arrays, *Nano Energy*, vol. **38**, pp. 59–65, 2017.

Wen, R., Xu, S., Lee, Y.C., and Yang, R., *Capillary Evaporation and Boiling Heat Transfer on Hybrid Wicking Structures*, International Heat Transfer Conference Digital Library, New York: Begell House Inc., 2018.

Wu, H.Y. and Cheng, P., Visualization and Measurements of Periodic Boiling in Silicon Microchannels, *Int. J. Heat Mass Transf.*, vol. **46**, no. 14, pp. 2603–2614, 2003.

Zhang, W., Hibiki, T., Mishima, K., and Mi, Y., Correlation of Critical Heat Flux for Flow Boiling of Water in Mini-Channels, *Int. J. Heat Mass Transf.*, vol. **49**, nos. 5–6, pp. 1058–1072, 2006.

Zhou, J., Vacca, A., and Casoli, P., A Novel Approach for Predicting the Operation of External Gear Pumps under Cavitating Conditions, *Simul. Model Pract. Theory*, vol. **45**, pp. 35–49, 2014.

Zou, A., Fundamentals of Microlayer Evaporation and Its Role on Boiling Heat Transfer Enhancement, PhD, Syracuse University, 2015.

Zou, A., Gupta, M., and Maroo, S.C., Origin, Evolution, and Movement of Microlayer in Pool Boiling, *J. Phys. Chem. Lett.*, vol. **9**, no. 14, pp. 3863–3869, 2018.

Zou, A., Singh, D.P., and Maroo, S.C., Early Evaporation of Microlayer for Boiling Heat Transfer Enhancement, *Langmuir*, vol. **32**, no. 42, pp. 10808–10814, 2016.

ZutaCorp, Enhanced Nucleation Developing Technology Descriptions, from https://zutacore.com/solutions, (n.d.).

APPENDIX A. DETAILS OF PIEZOS POWER CONSUMPTION

At imposed ultrasonic frequencies, the piezos in Fig. 1 are activated near their 3-3 thickness mode crystal vibration frequencies. These signals are then amplified by a suitable R-f amp (Yektasonics via APC, Inc.) yielding the output voltage V_{out} (t) indicated in Fig. 1. Again, V_{out} (t) as well as the impedance Z (see Fig. 10) of the piezos are measured after the test section and heater block are assembled into the flow loop. The V_{out} (t) are measured here over 20 μs durations and sampled by a Picoscope at 125 MHz. These measurements account for the various electromechanical coupling of the piezos to the structure. The antiresonance frequency ($f_{AR} \cong 4.73$ MHz), as identified in Fig. 10, is chosen as the ultrasonic frequency f_P used in the output of the signal generator in Fig. 1(c). Selecting $f_P = f_{AR}$ in Fig. 1 leads to the best energy-efficient resonant performance of the piezos because then the R-f amp's electric circuit sees a circuit model (APC International, 2002) that is mostly reactive (i.e., with low electrical resistance). The modulation frequency f_M is tested here in the range of $0.8\ \text{Hz} \le f_M \le 500\ \text{Hz}$, though it could be chosen anywhere in the range of $100\ \text{Hz} \le f_M \le 10\ \text{kHz}$.

It turns out that a piezo's output voltage, V_{out} (t), is not purely sinusoidal, and therefore is not made up of either one or a sum of multiple sinusoids of frequencies f_j. Therefore, if $\left|V_{out}\right|_{FFT-f_j}$ represents the magnitude of the fast/discrete Fourier transform (FFT) of V_{out} (t) corresponding to a sinusoidal frequency f_j and Z is the complex impedance (with $Z = |Z|_{f_j} * e^{i\phi_Z}$ at frequency f_j where **i** is the imaginary number) of one of the piezos PZ, the well-known complex power consumed formula (Rawlins, 2000) given in Eq. (A.1) cannot be used directly.

$$P_{PZ,\text{Complex } f=f_j} \equiv P_{PZ-t} + \mathbf{i}P_{PZ-t-\text{reactive}} \equiv \frac{\left|V_{out}\right|^2_{FFT-f_j}}{2\,|Z|_{f_j}} \cdot e^{i\phi_Z} \tag{A.1}$$

$$\text{Re}\left[P_{PZ,\text{ Complex } f=f_j}\right] \equiv P_{PZ-t} \tag{A.2}$$

$$\text{psd}(f) \equiv \frac{|V_{out}|^2_{FFT-f}(f)}{2\left|Z(f)\right|} \tag{A.3}$$

The real part of Eq. (A.1) as given in Eq. (A.2) and the associated delta function result for the power spectral density function defined in Eq. (A.3) is only valid for a pure sinusoid of frequency f_j. But the dissipative power of interest of a more general and not purely sinusoidal V_{out} (t) obtained from measurements in Fig. 1 is to be used. For this, the usual approach is followed.

First, a power density function spectrum in Eq. (A.3) of the representative V_{out} (t) signal acquired through a Picoscope at a DAQ rate of 125 MHz and suitable time duration is obtained from the relevant $|V_{out}|_{FFT-f_j}$ (see representative MATLAB results in Fig. A.1(a)–A.1(b). The total complex power consumed $P_{PZ,Complex}$ is then computed using a suitable incremental frequency df and by Eq. (A.4) below:

$$P_{PZ-t,Complex} \equiv \int_0^{\infty \sim 10\,MHz} \frac{|V_{out}|^2_{FFT-f}(f)}{2|Z(f)|} \cdot e^{i\phi_Z} df \tag{A.4}$$

Next, the real part of Eq. (A.4), namely

$$Re\,[P_{PZ-t,Complex}] \equiv P_{PZ-t} \tag{A.5}$$

is the total dissipative power of interest, as shown in Fig. A.1(c) in this paper. As seen in Fig. (A.1a–A.1b), the piezos excitation frequency $f_P \cong 4.73$ MHz couples mostly with a subharmonic frequency $f_{P-sub} \cong 2.7$ MHz. Typically, it is expected that as the signal generator voltage is increased, the piezos would start pumping progressively larger amounts of energy into this substructural mesh-wire's ultrasonic vibrations (see Fig. 4) associated with the subharmonic frequency $f_{P-sub} \cong 2.7$ MHz. This is the case when the signal generator voltage amplitude of 4 V in Fig. A.1 goes to 6 V in Fig. A.1(b). The substructure's ultrasonic vibration power (P_{PZ-R}) defined in Eq. (A.6) below for the subharmonic frequency $f_{P-sub} \cong 2.7$ MHz can be studied with the 3D Laser Vibrometer used for Fig. 5, but this is not the focus here. It suffices to note that the substructural dissipative power P_{PZ-R} (expected to be less than the total piezo dissipative power P_{PZ-t}) is given by

$$P_{PZ-R} \cong Re\left[\int_{f_{P-sub-L}}^{f_{P-sub-R}} psd(f) \cdot df\right] \tag{A.6}$$

These measurements are not entirely dependent on the accuracy of the dissipative power computations from Eqs. (A.4)–(A.6), which are likely within 1% of the computed values. They

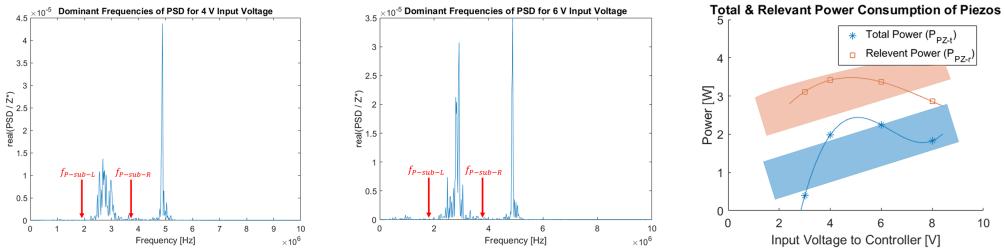

(a) **(b)** **(c)**

FIG. A.1: The power density function spectrum $psd(f) \equiv |V_{out}|^2_{FFT-f}(f)/2|Z(f)|$ of the representative output voltage V_{out} (t). (a) This psd(f) graph is for the 4 V amplitude of the signal generator signal in Fig. 1(c). (b) This psd(f) graph is for the 6 V amplitude of the signal generator signal. (c) The total dissipative piezos powers P_{PZ-t} and the substructural ultrasonic vibration powers P_{PZ-R} curves for $f = f_{p\text{-}sub}$ are for several cases, including the ones in (a)–(b), for the microstructure used and defined in subsection 3.2.2.

also depend on the stability of the diffusion-bonded microstructure used in the experiment. Stability can be affected by slippages and breakages of some of the bonds throughout the experiment, especially the more unstable bonds with $p_x \approx 0$ μm and $p_y \approx 0$ μm between layers 2 and 3 of Fig. 3(a) used in this experiment. As a result of this, the total power, P_{PZ-t}, and the substructure ultrasonic vibration power P_{PZ-R} curves in Fig. A.1(c) are nonmonotone with respect to driving input signal voltage. These powers are expected to become monotone (as indicated in shaded regions of Fig A.1c) in future experiments, which are planned for more stable microstructures that are less prone to slippages. The piezos excitation frequency $f_P \cong 4.73$ MHz couples mostly with a subharmonic frequency $f_{P-sub} \cong 2.7$ MHz in Figs. A.1(a)–A.1(b), where an increasing amount of dissipative power P_{PZ-R} computed by Eq. (A.6) is expected to be consumed.